Estimating the water-leaving albedo from ocean color

Xiaolong Yu [1*], Zhongping Lee [2], Shaoling Shang [1], Menghua Wang [3], Lide Jiang [3,4]

[1] State Key Laboratory of Marine Environmental Science, College of Ocean and Earth Sciences, Xiamen University, Xiamen 361101, China

[2] School for the Environment, University of Massachusetts Boston, Boston, MA 02125, USA

[3] NOAA Center for Satellite Applications and Research, College Park, MD 20740, USA

[4] Cooperative Institute for Research in the Atmosphere (CIRA), Colorado State University, Fort Collins, CO 80523, USA

*corresponding authors: xlyu@xmu.edu.cn

Abstract:

Water-leaving albedo (α_w), defined as the ratio of water-leaving irradiance to downwelling irradiance just above the surface, is a major component of ocean surface albedo (α) but has long been ignored or underrepresented. A semi-analytical scheme based on inherent optical properties (IOPs), termed IOPs-α_w, is proposed in this study to estimate spectral $\alpha_w(\lambda)$ from ocean color measurements. Evaluations with numerical simulations of radiative transfer show that IOPs-α_w outperforms the conventional scheme based on chlorophyll-a (Chl) concentration. The median absolute percentage difference (MAPD) of derived $\alpha_w(\lambda)$ from IOPs-α_w is generally less than 3% in the blue-green spectral domain, in comparison to MAPD of over 40% for estimated $\alpha_w(\lambda)$ from the Chl-based scheme. IOPs-α_w is later implemented to monthly composite data of the Visible Infrared Imaging Radiometer Suite (VIIRS) and reasonable spatial distributions and seasonal patterns of $\alpha_w(\lambda)$ are obtained. In particular, broadband α_w in the visible domain, termed α_{w_VIS}, obtained via IOPs-α_w is over 50% higher than the previous estimation by the Chl-based scheme in most oceanic waters. Furthermore,

this study concludes that water-leaving albedo could contribute up to 20% to α in oceanic waters under low solar-zenith angles. Thus, we suggest that neither the spatial variability of α_{w_VIS} nor the contribution of α_{w_VIS} to α shall be neglected, and it is necessary to incorporate IOPs-α_w into current parameterizations of α in the coupled ocean-atmosphere and climate models.

Keywords: water-leaving albedo, ocean surface albedo, inherent optical properties, BRDF, ocean color, VIIRS.

1. Introduction

Ocean is the most important heat buffer on Earth and plays a key role in modulating the coupled ocean-atmosphere system by reflecting and absorbing solar energy (Abraham et al., 2013; Henderson-Sellers and Wilson, 1983). A fundamental parameter to quantify the amount of ocean-absorbed solar energy is the ocean surface spectral albedo, $\alpha(\lambda)$, which is defined as the ratio of spectral upwelling plane irradiance, $E_u(z = 0^+, \lambda)$, to spectral downwelling plane irradiance, $E_d(z = 0^+, \lambda)$, just above the sea surface that is indicated by $z = 0^+$, and λ refers to light wavelength in vacuum (Payne, 1972). The units of spectral irradiance are W m^{-2} nm^{-1}. Note that the in-water biogeochemical processes such as photosynthesis or photolysis would affect $\alpha(\lambda)$ (Hense et al., 2017), thus variations in $\alpha(\lambda)$ could imply the changes in the primary production and ocean carbon uptake (Behrenfeld and Falkowski, 1997; Lee et al., 1996). In addition, the integral of $\alpha(\lambda)$ over the spectrum of 200–3000 nm weighted by $E_d(z = 0^+, \lambda)$, termed the broadband ocean surface albedo (α_{broad}), is of particular interest to the coupled ocean-atmosphere models for the determination of solar heating in the upper ocean and

radiation budget in the atmosphere (Faizal and Rafiuddin Ahmed, 2011; Jin et al., 2004). Therefore, accurate quantification of $\alpha(\lambda)$ is strongly desired.

The majority of peer-reviewed studies on earth albedo focused on land, cloud, ice, and snow. Studies of ocean surface albedo are much less documented, which is largely attributed to the perception that α_{broad} is considered a constant or can be parameterized with simple terms (Bender et al., 2006; Gupta et al., 1999). For instance, many earlier schemes assumed that α_{broad} is only dependent on the solar-zenith angle (Briegleb et al., 1986; Taylor et al., 1996), as they deemed the surface-reflected solar radiation dominated the upwelling irradiance. Some others incorporated wind information based on observations and theoretical analysis (Cox and Munk, 1954; Hansen et al., 1983; Jin et al., 2002), especially for rough sea surfaces with wind-driven foams and whitecaps (Koepke, 1984; Li et al., 2006). Scattering of solar radiation within the water column was also recognized to contribute to upwelling irradiance (see Fig. 1) (Chang and Dickey, 2004; Jin et al., 2002; Ohlmann et al., 2000; Payne, 1972), but the incorporation of water-leaving radiation to the quantification of $\alpha(\lambda)$ has long been ignored until recently (Feng et al., 2016; Jin et al., 2011; Séférian et al., 2018).

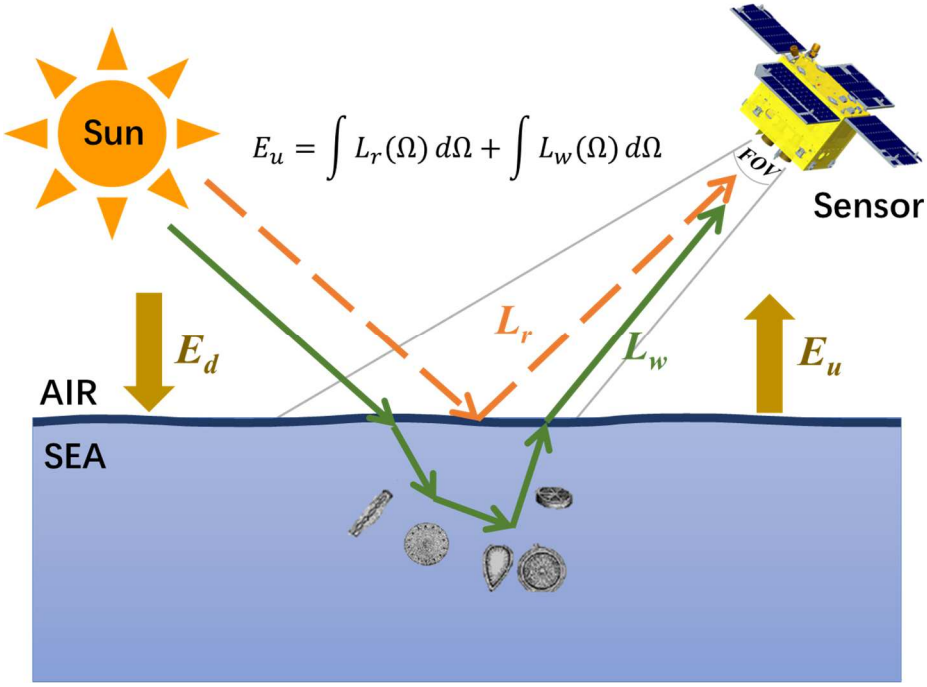

Fig. 1. Schematic pathways of the surface-reflected radiance (L_r) and the water-leaving radiance (L_w), the two components of upwelling irradiance (E_u). The symbol Ω refers to the angle dependencies of L_r and L_w. Note that this is a simplified plot that does not specifically show various light scattering processes from water and atmosphere.

The contribution of light scattering in the water column to $\alpha(\lambda)$, termed water-leaving albedo $\alpha_w(\lambda)$, is defined as the ratio of water-leaving irradiance $E_w(\lambda)$ to $E_d(z = 0^+, \lambda)$. Theoretically, $E_w(\lambda)$ can be calculated if the water-leaving radiance ($L_w(\lambda)$, in W m^{-2} nm^{-1} sr^{-1}, see Fig. 1), as well as its angular distribution, are known (Mobley, 1994; Mobley et al., 1993). Generally, $L_w(\lambda)$ varies with seawater inherent optical properties (IOPs, i.e., absorption and scattering coefficients) and solar-sensor geometry, while its angular variation can be represented by a bidirectional reflectance distribution function (BRDF) (Morel and Gentili, 1991; Morel and Gentili, 1993; Morel and Gentili, 1996). Based on the "Case-1" water assumption (Morel and Prieur, 1977), IOPs can be parameterized by the concentration of phytoplankton pigment, mostly the chlorophyll-a (Chl, in mg/m^3) (Morel and Maritorena, 2001). The "Case-1" water assumption was commonly adopted by the previous schemes for

78 the estimation of $\alpha_w(\lambda)$ (Feng et al., 2016; Jin et al., 2011; Séférian et al., 2018).

79 However, there is no clear quantitative boundary of "Case-1" waters (IOCCG, 2000), and
80 the covariance between phytoplankton and co-existing optically significant constituents, such
81 as colored dissolved organic matter (CDOM) and non-algal particulate matter, could be
82 complicated even in the open ocean (Bricaud et al., 1981; Lee and Hu, 2006; Mobley et al.,
83 2004). More importantly, the validity of IOPs inferred from Chl relies heavily on the
84 Chl-specific absorption and Chl-specific backscattering coefficients, which varies greatly in
85 the global ocean (Bricaud et al., 1995; Huot et al., 2008; Loisel and Morel, 1998; Reynolds et
86 al., 2001; Stramska et al., 2003). Consequently, large uncertainties of inferred IOPs from Chl
87 will be propagated to the estimated $\alpha_w(\lambda)$, especially when remotely sensed Chl is also subject
88 to large uncertainties (Carder et al., 1999; O'Reilly et al., 1998). Further, for optically complex
89 waters where the covariance between Chl and IOPs of other seawater constituents no longer
90 holds, $\alpha_w(\lambda)$ cannot be estimated from the above schemes. As an alternative, Feng et al. (2016)
91 empirically related $\alpha_w(\lambda)$ to remote sensing reflectance ($R_{rs}(\lambda)$, in sr^{-1}), but such empirical
92 relationships are always data-driven and have limited applicability. Because IOPs are the
93 essential properties to reconstruct angular $L_w(\lambda)$ and can be directly derived from ocean color
94 (Gordon et al., 1988; Lee et al., 2002; Loisel and Stramski, 2000; Maritorena et al., 2002;
95 Roesler and Perry, 1995; Shi and Wang, 2019), a scheme of estimating $\alpha_w(\lambda)$ based on IOPs
96 would be preferred.

97 Lee et al. (2011) developed an IOPs-centered system to correct the angular effects of
98 $L_w(\lambda)$, which, in turn, can be used to model the angular $L_w(\lambda)$ from known IOPs. Based on Lee

et al. (2011), we propose a semi-analytical scheme, termed IOPs-α_w, to estimate $\alpha_w(\lambda)$ from $R_{rs}(\lambda)$. The developed scheme is first evaluated with radiative transfer simulated datasets using HydroLight and then compared with previous schemes based on Chl or $R_{rs}(\lambda)$. The sensitivity of IOPs-α_w to wind speed, particle scattering phase function, Raman scattering, and chlorophyll fluorescence are also investigated. IOPs-α_w is further applied to the Visible Infrared Imaging Radiometer Suite (VIIRS) monthly composite data to demonstrate the global distribution of $\alpha_w(\lambda)$ and the seasonal pattern of the broadband α_w in the visible domain (α_{w_VIS}). Finally, the contribution of α_{w_VIS} to α_{broad} is discussed.

2. Data and Methods

2.1. Schemes for the spectral water-leaving albedo

As illustrated in Fig. 1, the upwelling irradiance has two components, thus the ocean surface albedo is also composited of the surface-reflected component and water-leaving component. Here we term the water-leaving component as the spectral water-leaving albedo ($\alpha_w(\lambda)$), which is expressed as

$$\alpha_w(\lambda,\theta_s)=\frac{E_w(\lambda,\theta_s)}{E_d(z=0^+,\lambda,\theta_s)}, \quad (1)$$

where $E_w(\lambda, \theta_s)$ is the irradiance leaving the water surface contributed by photons scattered within the water column (i.e., a weighted sum of all the water-leaving radiance $L_w(\lambda)$), $E_d(z = 0^+, \lambda, \theta_s)$ is the downward irradiance just above the sea surface, and θ_s is the solar-zenith angle. For remote sensing platforms, $E_w(\lambda, \theta_s)$ cannot be measured directly, but can be calculated based on its relationship with $L_w(\lambda)$, which varies with angular geometry, i.e., solar-zenith angle θ_s, viewing-zenith angle θ_v, and the viewing azimuth angle to the solar plane φ.

Theoretically, $E_w(\lambda, \theta_s)$ is the integral of $L_w(\lambda, \theta_s, \theta_v, \varphi)$ over all viewing angles, which correspond to all upwelling directions that photons travel, weighted by the cosine of θ_v. In the following, the three angles (θ_s, θ_v, and φ) are collectively represented as Ω unless further clarification is required. Thus, $E_w(\lambda, \theta_s)$ can be expressed as

$$E_w(\lambda,\theta_s)=\int_0^{2\pi}\int_0^{\pi/2} L_w(\lambda,\theta_s,\theta_v,\varphi)\cos\theta_v \sin\theta_v d\theta_v d\varphi. \quad (2)$$

In ocean color remote sensing, remote sensing reflectance $R_{rs}(\lambda)$ is defined as the ratio of $L_w(\lambda, \theta_s, \theta_v, \varphi)$ to $E_d(z = 0^+, \lambda, \theta_s)$

$$R_{rs}(\lambda,\theta_s,\theta_v,\varphi)=\frac{L_w(\lambda,\theta_s,\theta_v,\varphi)}{E_d(z=0^+,\lambda,\theta_s)}. \quad (3)$$

By substituting Eqs. (2) and (3) into Eq. (1), one can easily obtain

$$\alpha_w(\lambda,\theta_s)=\int_0^{2\pi}\int_0^{\pi/2} R_{rs}(\lambda,\theta_s,\theta_v,\varphi)\cos\theta_v \sin\theta_v d\theta_v d\varphi. \quad (4)$$

For efficient computation, the angular distribution of $L_w(\lambda, \theta_s, \theta_v, \varphi)$ is assumed azimuthally symmetric about the solar plane in this study, which is also the default setting in HydroLight (Mobley and Sundman, 2016). Thus, one can rewrite Eq. (4) as

$$\alpha_w(\lambda,\theta_s)=2\int_0^{\pi}\int_0^{\pi/2} R_{rs}(\lambda,\theta_s,\theta_v,\varphi)\cos\theta_v \sin\theta_v d\theta_v d\varphi. \quad (5)$$

Therefore, the key to estimate $\alpha_w(\lambda, \theta_s)$ is to obtain the angular distribution of $R_{rs}(\lambda, \theta_s, \theta_v, \varphi)$ for θ_v ranging from 0° to 90° and φ from 0° to 180°. For simplicity, the angular dependency of all radiometric terms is omitted in the following text unless further clarification is required.

2.1.1. IOPs-based scheme (IOPs-α_w)

To explicitly separate the phase function effects resulted from molecular and particulate

scattering, the angular distribution of $R_{rs}(\lambda)$ can be modeled from IOPs (Lee et al., 2011)

$$R_{rs}(\lambda,\Omega)=\left(G_0^w(\Omega)+G_1^w(\Omega)\frac{b_{bw}(\lambda)}{\kappa(\lambda)}\right)\frac{b_{bw}(\lambda)}{\kappa(\lambda)}+\left(G_0^p(\Omega)+G_1^p(\Omega)\frac{b_{bp}(\lambda)}{\kappa(\lambda)}\right)\frac{b_{bp}(\lambda)}{\kappa(\lambda)}, \quad (6)$$

where $b_{bw}(\lambda)$ and $b_{bp}(\lambda)$ are the backscattering coefficients of pure seawater and particles, respectively. $\kappa(\lambda)$ is the sum of total absorption coefficient $a(\lambda)$ and backscattering coefficient $b_b(\lambda)$ (i.e., $\kappa(\lambda) \equiv a(\lambda) + b_b(\lambda)$), with $b_b(\lambda) = b_{bw}(\lambda) + b_{bp}(\lambda)$. $G_0^w(\Omega)$, $G_1^w(\Omega)$, $G_0^p(\Omega)$, and $G_1^p(\Omega)$, collectively termed G, are model coefficients that are dependent on angular geometry and assumed to be independent of IOPs and wavelength (Lee et al., 2011). The values of G can be retrieved from a look-up-table (LUT), termed G-LUT, for given angular geometry. Although a G-LUT was provided in Lee et al. (2011), we updated this LUT following the same approach in Lee et al. (2011) by expanding viewing angles and seawater IOPs using the simulated dataset in this study (described in Section 2.2). Specifically, G-LUT in Lee et al. (2011) excludes scenarios with large viewing- and solar-zenith angles (i.e., $\theta_v > 70°$ and $\theta_s > 75°$), which need to be expanded for more accurate estimation of $\alpha_w(\lambda)$, although $R_{rs}(\lambda)$ of extremely large angles contribute much less to $\alpha_w(\lambda)$ due to the cosine weighting. Also, the dataset of this study includes more optically complex waters, thus the resultant G-LUT could have broader applicability.

With known G values, the remaining unknowns to compute angular $R_{rs}(\lambda)$ are $a(\lambda)$ and $b_b(\lambda)$ as shown in Eqs. (5) and (6). Following the concept of the quasi-analytical algorithm (QAA) (Lee et al., 2002), $a(\lambda)$ and $b_b(\lambda)$ can be determined algebraically by solving Eq. (6) (detailed solutions are given in Eqs. (15)-(20) in Lee et al. (2011)). Note that the latest update (version 6) of QAA, available at

160 http://www.ioccg.org/groups/Software_OCA/QAA_v6_2014209.pdf, is incorporated into the
161 IOP inversion algorithm, which is hereafter termed QAA_Lee11.

162 The absorption and backscattering coefficients of pure seawater, $a_w(\lambda)$ and $b_{bw}(\lambda)$, are
163 considered known and can be acquired from the literature. The recent International Ocean
164 Colour Coordinating Group (IOCCG) protocol recommends the use of Morel et al. (2007) for
165 $a_w(\lambda)$ up to 420 nm and Pope and Fry (1997) for $a_w(\lambda)$ above 420 nm (IOCCG Protocol Series,
166 2018). However, there are still debates on the "true" value of the absorption coefficients of
167 "pure" water, especially "pure" seawater for oceanic environments. Our previous assessments
168 show that the $a_w(\lambda)$ values of Lee et al. (2015) could be closer to the "true" absorption
169 coefficient of pure seawater in the 350–550 nm domain (Wei et al., 2021; Yu et al., 2019b).
170 Thus, $a_w(\lambda)$ values in this paper adopted those from Lee et al. (2015) for 400 – 550 nm and
171 those from Pope and Fry (1997) for 550 nm and above. Values of $b_{bw}(\lambda)$ are taken from Zhang
172 et al. (2009), which is computed with salinity of 35 PSU and temperature of 20°C. The
173 proposed scheme is hereafter referred to as IOPs-α_w, which requires inputs of $R_{rs}(\lambda)$ and Ω,
174 where $R_{rs}(\lambda)$ is used to derive IOPs and Ω is used to retrieve G values from the G-LUT.

175 2.1.2. Chl-based scheme (Chl-α_w)

176 In a previous α_w scheme (Feng et al., 2016), angular $L_w(\lambda)$ is expressed as (Gordon et al.,
177 1988; Morel and Gentili, 1993)

178 $$\frac{L_w(\lambda,\Omega)}{E_d(\lambda,\theta_s)}=\left\{\frac{(1-\bar{\rho})[1-\rho(\theta_s',\theta_v)]}{(1-\bar{r}R)n^2}\right\}\frac{f(\theta_s)}{Q(\theta_s',\theta_v,\varphi)}\frac{b_b(\lambda)}{a(\lambda)}, \quad (7)$$

179 where $\bar{\rho}$ is the air-water Fresnel reflectance at the interface for the whole downwelling

irradiance (Sun + sky) above the surface, $\rho(\theta_s^{'}, \theta_v)$ is the internal Fresnel reflectance for the associated directions $(\theta_s^{'}, \theta_v)$, with $\theta_s^{'}$ the corresponding refracted zenith angle in the water. $\bar{r}$ is the water-air Fresnel reflectance for the whole diffuse upwelling irradiance, R is the irradiance reflectance just beneath the surface, and n (= 1.34) is the refractive index of water. For simplicity, the reflection-refraction term within the braces is replaced by $\Re$. Q is the bidirectional function, and f is the model factor that governs the magnitude of R with $R=f \times b_b/a$. By substituting Eq. (3) with Eq. (7), one can rewrite a simple expression to describe angular $R_{rs}(\lambda)$

$$R_{rs}(\lambda,\Omega) = \Re \times \frac{f}{Q} \times \frac{b_b(\lambda)}{a(\lambda)}. \quad (8)$$

Thus, $\Re$ and f/Q at different solar-sensor geometry are required to compute angular $R_{rs}(\lambda)$. Note that $\Re$ is slightly dependent on wind speed (w, m/s), particularly for large solar-sensor zenith angles (Morel et al., 2002; Wang, 2006). In this study, $\Re$ is first computed following the LUT provided in Fig. 5 in Gordon (2005) and later corrected for the solar-zenith angle effects (Wang, 2006). LUT for f/Q is extracted from Eq. (B4) and Table 3 of Morel et al. (2002) for Chl ranging between 0.03 and 10 mg/m^3 and θ_s ranging between 0 and 87.5°. For input Chl outside the range of 0.03 to 10 mg/m^3, the closest boundary Chl is used to retrieve f/Q value from the LUT, following the same practice as l2gen in the Sea-viewing Wide Field-of-view Sensor (SeaWiFS) Data Analysis System (SeaDAS).

For schemes based on Chl (Feng et al., 2016; Jin et al., 2011; Séférian et al., 2018), IOPs are estimated from Chl using Eqs. (13) and (16) of Morel and Maritorena (2001), with Chl first obtained from satellite-observed $R_{rs}(\lambda)$ using the ocean color index (OCI) algorithm (Hu

et al., 2012; Wang and Son, 2016), which is a merged algorithm of the band-ratio OCx algorithm (O'Reilly et al., 1998) and the color index (CI) algorithm (Hu et al., 2012). The scheme proposed in this section is hereafter denoted as Chl-α_w. To summarize, Chl-α_w requires input $R_{rs}(\lambda)$, Ω and w, where $R_{rs}(\lambda)$ is used to derive Chl, while Ω and w, along with derived Chl, are used to retrieve f/Q and $\Re$ at different Ω to model the angular $R_{rs}(\lambda, \Omega)$.

2.1.3. The Jin11 scheme

Jin et al. (2011) parameterized $\alpha_w(\lambda)$ as two separate components contributed by direct and diffuse irradiance incident upon the sea surface, which is hereafter termed the Jin11 scheme. With the consideration of multiple reflections of the upwelling irradiance at the water-air interface, Jin et al. (2011) expressed the direct $\alpha_w(\lambda)$, termed $\alpha_{w\_dir}(\lambda)$, as

$$\alpha_{w\_dir}(\lambda,\theta_s)=\left\{\frac{(1-\bar{r})(1-\bar{\rho})}{(1-\bar{r}R)}\right\}f(\theta_s)\frac{b_b(\lambda)}{a(\lambda)}. \quad (9)$$

Here, both $\bar{r}$ and $\bar{\rho}$ (notations explained in Section 2.1.2) are corrected for the impacts of wind speed (see Eqs. (1) and (7) in Jin et al. (2011)). Different from Chl-α_w, the BRDF effect is ignored in Jin11, while f in Eq. (9) is expressed as a function of IOPs and θ_s following Eq. (14) of Morel and Gentili (1991). Consistent with Chl-α_w, IOPs in Eq. (9) are parameterized by Chl, which is derived using the OCI algorithm. The diffuse component of $\alpha_w(\lambda)$, termed $\alpha_{w\_dif}(\lambda)$, is equivalent to $\alpha_{w\_dir}(\lambda)$ with θ_s as 47.47°, which is the effective angle to account for the diffuse contribution of the incident irradiance (Morel and Gentili, 1991). $\alpha_w(\lambda)$ is then simply a linear combination of $\alpha_{w\_dif}(\lambda)$ and $\alpha_{w\_dir}(\lambda)$, weighted by the fraction of diffuse downwelling irradiance (f_{dif}) in the total downwelling irradiance,

$$\alpha_w(\lambda,\theta_s)=(1-f_{dif})\alpha_{w\_dir}(\lambda,\theta_s)+f_{dif}\alpha_{w\_dif}(\lambda,\theta_s). \quad (10)$$

Note that f_{dif} depends on the atmospheric conditions, wavelength, and solar elevation, but it has a relatively small impact on the estimated $\alpha_w(\lambda)$ as the estimated $\alpha_{w\_dif}(\lambda)$ and $\alpha_{w\_dir}(\lambda)$ are overall comparable (difference within 20% for most waters in the simulated dataset of this study). Also, as discussed in Section 3.2.1, the major uncertainties of Jin11 are introduced by the Chl-IOPs relationship. Thus, we simply use a constant f_{dif} of 0.3, assuming zero cloud fraction (Kasten and Czeplak, 1980), for easy implementation of Jin11 in this study.

2.1.4. Empirical scheme (Feng16)

Given the complexity and computation cost of Chl-α_w, Feng et al. (2016) also related $\alpha_w(\lambda)$ empirically to nadir-viewed $R_{rs}(\lambda)$ using a quadratic equation (hereafter denoted Feng16),

$$\alpha_w(\lambda,\theta_s)=m_1(\lambda,\theta_s)(\pi R_{rs}(\lambda))^2+m_2(\lambda,\theta_s)(\pi R_{rs}(\lambda)), \quad (11)$$

where m_1 and m_2 are empirical coefficients that can be retrieved from a LUT for specific wavelengths and θ_s. Note that Feng et al. (2016) obtained the empirical coefficients in Eq. (11) by the least-squares fitting from a simulated dataset based on Eq. (7) with different inputs of Chl and w. Therefore, Feng16 can also be treated as a variant of the Chl-based scheme. In this study, we only evaluate Feng16 for the estimated $\alpha_w(410)$ at $\theta_s = 30°$, as empirical coefficients are only available for this case, with m_1 and m_2 as −6.5 and 0.87, respectively (see Fig. 3 of Feng et al. (2016)).

2.1.5. Scheme based on normalized water-leaving reflectance (ρ_w-α_w)

Assuming an isotropic distribution of water-leaving radiance $L_w(\lambda)$, $E_w(\lambda)$ would equal to $\pi L_w(\lambda)$ and $\alpha_w(\lambda)$ can be simply calculated as $\pi R_{rs}(\lambda)$. Note that satellite $R_{rs}(\lambda)$ products are corrected to $R_{rs}(\lambda)$ viewed at nadir with the Sun at the zenith (Gordon and Wang, 1994), the estimated $\alpha_w(\lambda)$ from satellite $R_{rs}(\lambda)$ would be equivalent to the normalized water-leaving reflectance $\rho_w(\lambda)$ (Wang, 2006). This scheme is hereafter referred to as ρ_w-α_w.

2.2. Simulated datasets via radiative transfer

Determination of $\alpha_w(\lambda)$ in the field is still challenging as there is no practical approach to separate water-leaving irradiance from the total upwelling irradiance. Numerical simulations of radiative transfer in the ocean with HydroLight code (Mobley and Sundman, 2016) solves the scalar radiative transfer equation and provides the angular distribution of water-leaving radiance (thus $E_w(\lambda)$) as the output, allowing evaluations of different $\alpha_w(\lambda)$ schemes (Chang and Dickey, 2004; Mobley and Sundman, 2016; Ohlmann et al., 2000). Note that HydroLight ignores the polarization state of radiance, it could introduce errors to the simulated radiances at various angles compared to that in the natural environment. However, the inaccuracies in the obtained irradiance from scalar radiative transfer can be negligible because the errors in the radiance tend to average out when radiance is integrated over all directions in the upper hemisphere. General HydroLight configurations are the same as that in Yu et al. (2021), where data are simulated using HydroLight 5.3 with the option of input IOPs by user-supplied total absorption ($a(\lambda)$) and attenuation ($c(\lambda)$) coefficients. The water column is assumed infinitely deep and homogeneous, and inelastic radiative processes (such as Raman scattering by water

261 molecules and chlorophyll fluorescence) are excluded. IOPs of pure seawater employ the
262 same values as that used in IOPs-α_w (see Section 2.1.1).

263 The input $a(\lambda)$ and $c(\lambda)$ are synthesized based on the 500 IOP data of IOCCG report #5
264 (IOCCG, 2006), where Chl ranges between 0.03 – 30.0 mg/m^3 and IOPs of water constituents
265 are determined randomly, with constraints, from Chl. Descriptive files for the IOPs synthesis,
266 referred to as the *datafile* hereafter, can be found at
267 https://www.ioccg.org/groups/OCAG_data.html. Different from that described in the *datafile*,
268 we deliberately increase the variation ranges of the absorption and backscattering coefficients
269 by non-algal particles in relatively productive waters so that the simulations will cover a
270 wider range of water types. Specifically, for simulations where input Chl is larger than 1
271 mg/m^3, p_1 in Eq. (6) of the *datafile*, defined as the ratio of non-algal particulate absorption
272 (often also referred to as detrital absorption) to phytoplankton absorption coefficient at 440
273 nm, is recalculated randomly between 0.1 and 2.6. In addition, p_4 in Eq. (14) of the *datafile*,
274 determining the ratio of non-algal particulate backscattering coefficient at 550 nm to [Chl]$^{0.766}$,
275 is recalculated randomly between 0.06 and 2.6. Other input data used in the HydroLight
276 simulations are listed below:

277 - Wavelength: 350 – 750 nm with 10 nm interval.
278 - $_s$: 8 values, 0° – 75° (15° increment), 80°, and 88°.
279 - w: 3 values, 5, 10, and 15 m/s.
280 - θ_v: 10 values, 0° – 80° (10° increment), and 87.5° (default in HydroLight).
281 - φ: 13 values, 0° – 180° (15° increment) (default in HydroLight).

Note that when viewed at nadir (i.e., $\theta_v = 0°$), φ is set to 0° in HydroLight configuration. Thus, the selected θ_v and φ values would result in 118 combinations of viewing geometries (i.e., 9 θ_v ×13 φ +1).

The default particle scattering phase function for HydroLight simulation is taken from Petzold (1972), with an effective particulate backscattering-to-scattering ratio of 1.83%. Thus, a total number of 12,000 simulations (i.e., 500 IOPs×8 θ_s×3 w) were obtained, which is hereafter referred to as *SynData*. To evaluate the impact of the scattering phase function on IOPs-α_w, HydroLight was run again with the same inputs except that the Fournier-Forand scattering phase function with a particulate backscattering-to-scattering ratio of 1% was used (Fournier and Forand, 1994), with the resultant dataset denoted as *SynData*-FF. The simulated spectral $R_{rs}(\lambda)$ in both *SynData* and *SynData*-FF datasets are shown in Fig. 2. Due to the modifications of p_1 and p_4 and different scattering phase functions used in this effort, spectral $R_{rs}(\lambda)$ in *SynData* (Fig. 2a) show elevated reflectance compared to $R_{rs}(\lambda)$ in the IOCCG (2006) dataset, suggesting that *SynData* is representative of broader water types and includes optically more complex waters.

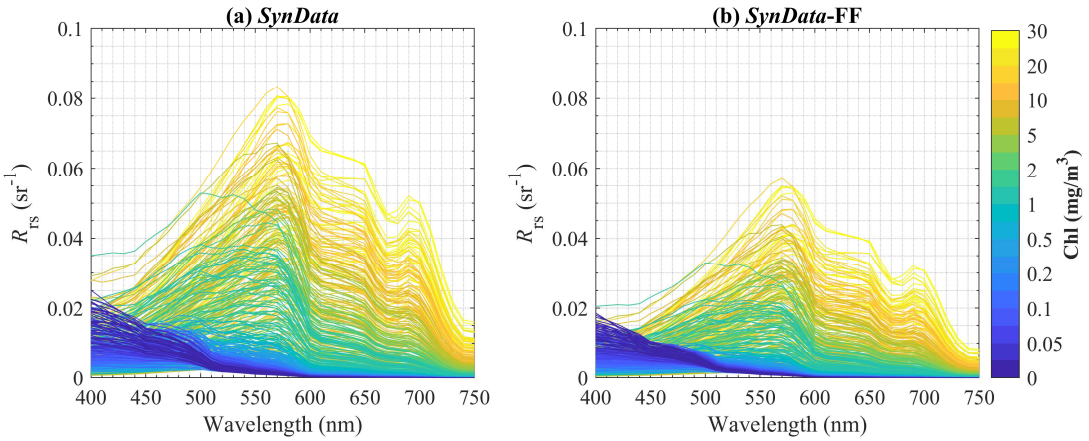

Fig. 2. Nadir-viewing spectral remote-sensing reflectance $R_{rs}(\lambda)$ simulated with HydroLight model using the IOP input data corresponding to different chlorophyll-a concentrations as indicated with the color bar scale and two different particle scattering phase functions where the Petzold average function is used in (a) and Fournier-Forand (1% particulate backscattering-to-scattering ratio) is used in (b). Only simulations for θ_s =30° and w = 5 m/s are shown as examples.

An additional dataset was simulated using the same HydroLight configuration as that in *SynData* but taking into consideration both Raman scattering and chlorophyll fluorescence. This new dataset is termed *SynData*-RF hereafter. Note that *SynData*-RF includes only 800 simulations, where the input IOPs ($a(\lambda)$ and $c(\lambda)$) were selected as every fifth data from the total 500 IOPs data in *SynData* and the wind speed w was set to 5 m/s (i.e., 100 IOPs×8 θ_s×1 w).

2.3. Broadband albedo

For hyperspectral data, the broadband albedo is simply the integral of spectral albedo weighted by $E_d(z = 0^+, \lambda)$ (Ohlmann et al., 2000). Thus, the broadband albedo depends on the wavelength ranges over which spectral albedo is integrated. This study focuses on the broadband α_w in the visible domain (i.e., 400–700 nm, the major range in ocean optics), which is hereafter referred to as α_{w_VIS}. Thus, α_{w_VIS} can be calculated following

$$\alpha_{w\_VIS} = \frac{\int_{400}^{700} \alpha_w(\lambda) E_d(0^+, \lambda)}{\int_{400}^{700} E_d(0^+, \lambda)}. \quad (12)$$

For satellite observations, broadband albedo can be empirically converted from narrowband albedo with empirical conversion coefficients (Liang, 2001),

$$\alpha_{w\_VIS} = \sum_{i=1}^{5} k_i \alpha_w(\lambda_i) + k_0, \quad (13)$$

where $\alpha_w(\lambda_i)$ is the narrowband albedo from satellite observation, k_i (i = 1 – 5) are conversion coefficients for corresponding spectral bands, and k_0 is a constant. The spectral bands and the values of k_i (i = 0–5) are dependent on the band configuration of different sensors. k_i (i = 0–5) can be derived using the least-squares fitting from known α_{w_VIS} and spectral $\alpha_w(\lambda)$. In this study, $\alpha_w(\lambda)$ from HydroLight outputs at 10 nm intervals are first interpolated to 1 nm intervals and then used to compute the known α_{w_VIS} using Eq. (12).

2.4 Evaluation metrics

Statistical measures are introduced to quantitatively evaluate the performance of $\alpha_w(\lambda)$ schemes, including the slope, coefficient of determination (R^2), the median absolute percentage difference (MAPD), and the *bias*. Slope and R^2 are calculated from linear regression using the Model-II regression (Laws, 1997), while MAPD and *bias* are defined as,

$$MAPD = median\left\{\left|\frac{y_i - x_i}{y_i}\right|\right\} \times 100\%,\ i = 1, 2, ...N \quad (14)$$

$$bias = median\left\{\frac{y_i - x_i}{y_i}\right\} \times 100\%,\ i = 1, 2, ...N \quad (15)$$

where x and y stand for the known and derived properties, respectively, N is the total number of samples used for metrics calculation.

3. Results

3.1 Evaluation of IOPs-α_w

We first applied the IOPs-α_w scheme to *SynData*, the same dataset used to update the *G*-LUT. Note that IOPs-α_w can be initiated with known $R_{rs}(\lambda)$ of any viewing angles, here we used the nadir-viewed $R_{rs}(\lambda)$, termed $R_{rs}(\lambda, \text{nadir})$, as input to derive IOPs from QAA_Lee11 for demonstration. The angular $R_{rs}(\lambda)$ can then be modeled following Eq. (6) using derived IOPs and the *G*-LUT. The scatterplots in Fig. 3 compare the estimated $\alpha_w(\lambda)$ from IOPs-α_w and the known $\alpha_w(\lambda)$ for five selected wavelengths (410, 440, 490, 550, and 670 nm), which represent the nominal wavelengths used in most satellite ocean color sensors. The known $\alpha_w(\lambda)$ (or reference) were calculated from angular $R_{rs}(\lambda)$ provided by HydroLight simulations following Eq. (5). Note that both the modeled angular $R_{rs}(\lambda)$ from IOPs-α_w and the known angular $R_{rs}(\lambda)$ from HydroLight outputs are only available at 118 viewing angles (i.e., 10 θ_v values from 0° – 87.5° and 13 φ values from 0° – 180°, see Section 2.2). As $\alpha_w(\lambda)$ is the integral of $R_{rs}(\lambda)$ of all viewing angles in the upwelling direction, prior to the integral of angular $R_{rs}(\lambda)$ via Eq. (5), we interpolated the 118 angular $R_{rs}(\lambda)$ to $R_{rs}(\lambda, \theta_v = 0° – 90°, \varphi = 0° – 180°)$ with θ_v and φ spacing at a step of 1°. The 'spline' method in MATLAB was used for the interpolation.

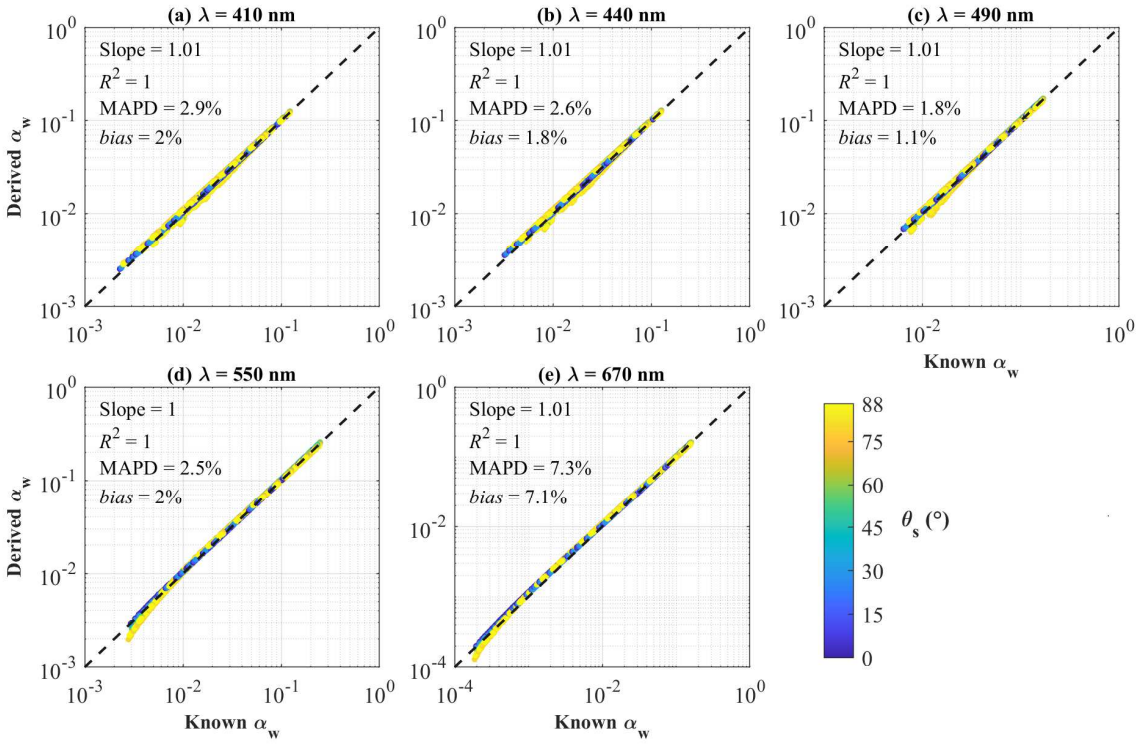

Fig. 3. Validation of derived spectral $\alpha_w(\lambda)$ using IOPs-α_w for *SynData*. The symbol color indicates the input solar-zenith angle.

As shown in Fig. 3, MAPD of the derived $\alpha_w(\lambda)$ by IOPs-α_w is less than 3% in the blue-green bands and is slightly larger for $\alpha_w(670)$ with MAPD of 7.3%. Statistics in Fig. 3 show that the derived $\alpha_w(\lambda)$ agrees excellently with known $\alpha_w(\lambda)$, suggesting the robustness of IOPs-α_w in all water types. The ~3% difference could be explained as the 'intrinsic' error introduced by *G*-LUT and the associated uncertainties in the IOPs derived from QAA_Lee11. As expressed in Eq. (5), $\alpha_w(\lambda)$ are a function of angular $R_{rs}(\lambda)$. Thus, the uncertainties of estimated $\alpha_w(\lambda)$ are, to the first order, dependent on the accuracy of modeled angular $R_{rs}(\lambda)$ from IOPs.

Given that QAA_Lee11 algebraically solves IOPs from the known $R_{rs}(\lambda$, nadir) (Eq. (6)), the modeled $R_{rs}(\lambda$, nadir) from derived IOPs would match exactly with the known $R_{rs}(\lambda$, nadir), which is independent of the uncertainties in the derived IOPs. However, there might be

discrepancies between the known and modeled $R_{rs}(\lambda)$ at other viewing angles, which is due to the inaccurate characterization of the bidirectional variation of $R_{rs}(\lambda)$ using derived IOPs and *G*-LUT. Statistics in Fig. 3 suggest that the uncertainties related to the bidirectional variation of $R_{rs}(\lambda)$ contribute less than ~3% error to the estimated $\alpha_w(\lambda)$ in the blue-green domain. The relatively larger uncertainties for $\alpha_w(670)$ are likely introduced by the *G*-LUT. Note that $R_{rs}(670)$ values are generally very small in most natural waters (see Fig. 2), while the optimized *G* values in *G*-LUT by least-squares fitting could be driven by larger $R_{rs}(\lambda)$ values at the blue-green bands. Therefore, the resultant *G* values would introduce larger uncertainties to the modeled angular $R_{rs}(670)$ and $\alpha_w(670)$. However, uncertainties in the estimated $\alpha_w(670)$ generally have negligible impacts on the calculated broadband α_w given its very small values in most natural waters.

3.2. Schemes inter-comparison

3.2.1. Evaluation of Chl-α_w and Jin11

For Chl-based schemes, we first derive Chl from the nadir-viewed $R_{rs}(\lambda)$ in *SynData* and subsequently derive IOPs from the obtained Chl. Spectral $\alpha_w(\lambda)$ are then estimated from the Chl-inferred IOPs via Chl-α_w and Jin11, respectively, with evaluation results at 440 and 550 nm presented in Fig. 4. Given the fact that uncertainties of modeled angular $R_{rs}(\lambda)$ from Chl-based schemes would determine the accuracy of the estimated $\alpha_w(\lambda)$, we also include the evaluation results of modeled nadir $R_{rs}(\lambda)$ from Chl-α_w in Fig. 4 for comparison. The modeled $R_{rs}(\lambda)$ were computed via Eq. (8) with the values of $\Re$ and f/Q taken from the corresponding LUTs for nadir viewing geometry.

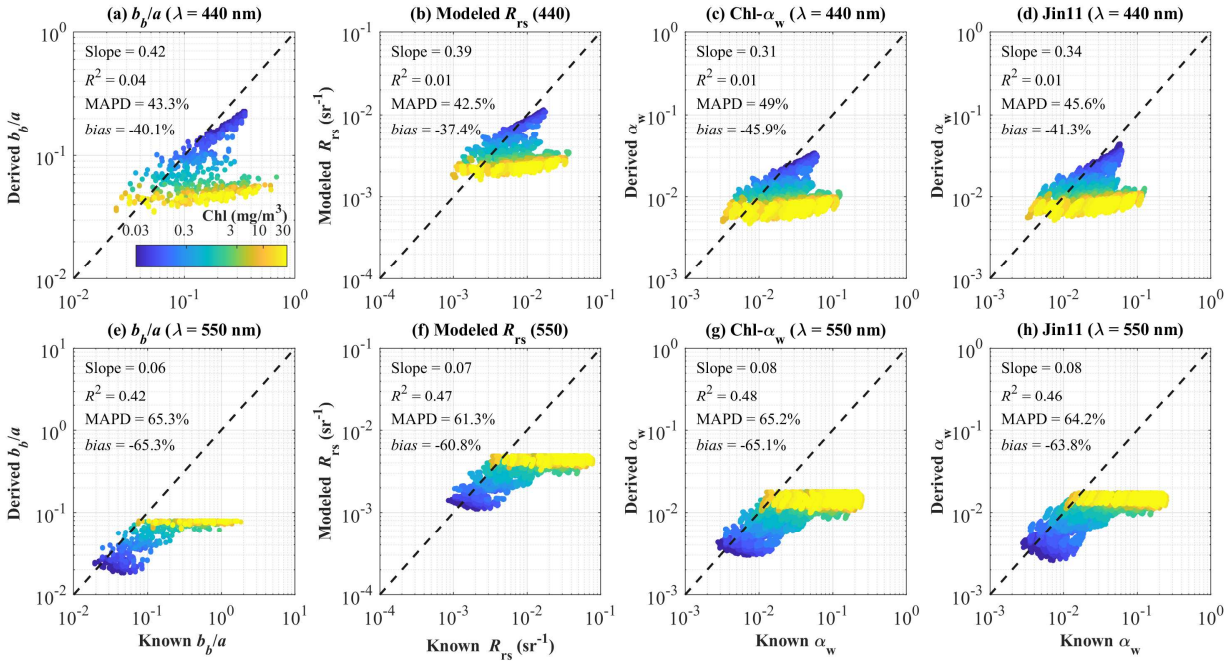

Fig. 4. Evaluation of Chl-inferred $b_b(\lambda)/a(\lambda)$ and modeled nadir-viewed $R_{rs}(\lambda)$ using Chl-α_w (left two panels) and estimated $\alpha_w(\lambda)$ using Chl-α_w and Jin11(right two panels). The symbol color indicates the corresponding input Chl for each simulation.

It can be found in Fig. 4 that the Chl-inferred $b_b(\lambda)/a(\lambda)$ from Chl differ greatly from the known values, with MAPD values as 43.3% and 65.3% for 440 and 550 nm, respectively. As angular $R_{rs}(\lambda)$ are a function of $b_b(\lambda)/a(\lambda)$ in both Chl-α_w and Jin11, large uncertainties of the estimated $\alpha_w(\lambda)$ from both schemes could be expected. For instance, the *bias* of the modeled nadir $R_{rs}(\lambda)$ at 440 and 550 nm from Chl-α_w are –37.4% and –60.8%, respectively (see Fig. 4b and Fig. 4f). Thus, uncertainties in the Chl-inferred IOPs could explain most of the uncertainties in the estimated $\alpha_w(\lambda)$.

The poor performance of Chl-based schemes in *SynData* is mainly attributed to the fact that for the same input Chl, synthetic IOPs in *SynData* are deliberately set to vary randomly, rather than following the "Case 1" empirical relationships reported in Morel and Maritorena (2001). Thus, large uncertainties in Chl-inferred IOPs are expected when compared to the

401 known values in *SynData*. In natural waters, variable Chl-IOPs relationships are also widely
402 documented as the concentration of phytoplankton pigment cannot solely explain the
403 variation of water IOPs, given the large variations of the Chl-specific absorption and
404 backscattering coefficients (Bricaud et al., 1995; Huot et al., 2008; Loisel and Morel, 1998;
405 Reynolds et al., 2001; Stramska et al., 2003). In addition, for remote sensing applications,
406 derived Chl itself is subject to uncertainties (Carder et al., 1999; O'Reilly et al., 1998), which
407 will be propagated to Chl-inferred IOPs. More importantly, there is no optical closure between
408 the simulated $R_{rs}(\lambda)$ from Chl-inferred IOPs and the $R_{rs}(\lambda)$ used to derive Chl (see Fig. 4b and
409 Fig. 4f), suggesting that the Chl-based schemes are lacking internal consistency.

410 3.2.2 Comparison with Feng16

411 Evaluation of Feng16 is also performed using *SynData*, with results shown in Fig. 5. As
412 described in Section 2.1.3, for a fair comparison, validation of estimated $\alpha_w(410)$ by IOPs-α_w
413 are screened for $\theta_s = 30°$.

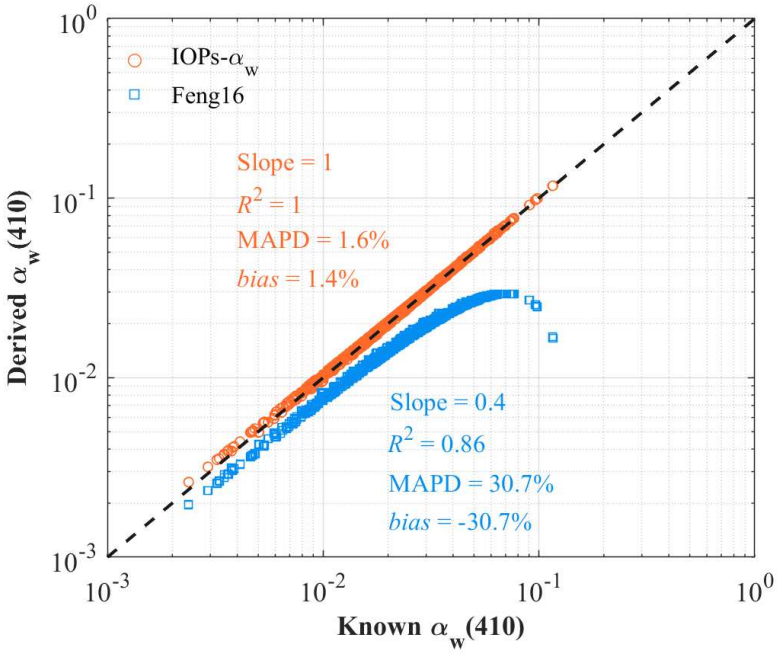

Fig. 5. Comparison of estimated $\alpha_w(410)$ by Feng16 and IOPs-α_w. Only simulations with input θ_s of 30° are considered here.

It is found that the empirical relationship developed in Feng et al. (2016) systematically underestimates $\alpha_w(410)$ for *SynData*, with a *bias* of −30.7%. The underestimation of Feng16 is likely because that their model coefficients are optimized based on a dataset simulated using Chl-α_w, which also systematically underestimates $\alpha_w(\lambda)$ (see Fig. 4). In contrast, $\alpha_w(410)$ derived from IOPs-α_w agrees very well with known values with a *bias* of only 1.4% and both the slope and R^2 are very close to 1. Thus, it can be concluded that empirical expressions between $\alpha_w(\lambda)$ and $R_{rs}(\lambda)$ will depend on the calibration dataset, which will then have limited applicability.

3.2.3 Evaluation of ρ_w-α_w

For the ρ_w-α_w scheme, $\alpha_w(\lambda)$ is simply estimated as $\pi R_{rs}(\lambda)$ with $R_{rs}(\lambda)$ takes as the nadir-viewed $R_{rs}(\lambda)$ from *SynData*, with evaluation results presented in Fig. 6. It can be found

that ρ_w-α_w outperforms both Chl-α_w and Feng16, with MAPD of estimated $\alpha_w(\lambda)$ generally less than 10% in the blue-green domain. However, the estimated $\alpha_w(\lambda)$ by ρ_w-α_w still have larger uncertainties than those of IOPs-α_w (see the comparison between Fig. 3 and Fig. 6). It is apparent that the performance of ρ_w-α_w is sensitive to the solar-zenith angle, where smaller $\alpha_w(\lambda)$ are observed at higher solar-zenith angle scenarios.

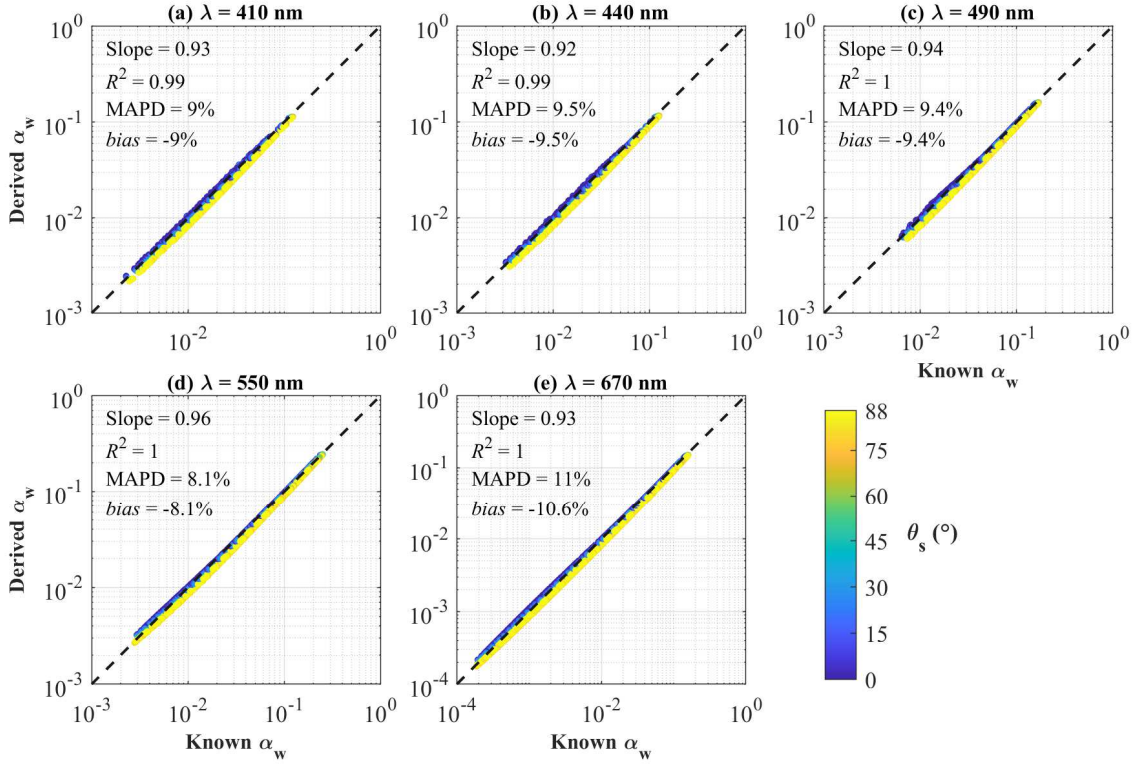

Fig. 6. Evaluation of ρ_w-α_w using *SynData* for wavelengths at 410, 440, 490, 550, and 670 nm. The symbol color indicates the input solar-zenith angle.

Given the fact that the bidirectionality of $R_{rs}(\lambda)$ cannot be neglected in most natural waters, it is of interest to evaluate the robustness of ρ_w-α_w when $R_{rs}(\lambda)$ of different viewing geometry is used as model input. Here, we simply use the 118 angular $R_{rs}(\lambda)$ in *SynData* to estimate $\alpha_w(\lambda)$ using the ρ_w-α_w scheme and then compare them with the known $\alpha_w(\lambda)$ values. The 118 angular $R_{rs}(\lambda)$ are the combinations of 10 θ_v and 13 φ (see Section 2.2 for details). For each combination of θ_v and φ, the *bias* of estimated $\alpha_w(\lambda)$ using $\pi R_{rs}(\lambda, \theta_v, \varphi)$ can be

calculated following Eq. (15) for all the 12000 simulations in *SynData*, with the *bias* of estimated $\alpha_w(\lambda)$ for all the 118 scenarios at five selected wavelengths shown in Fig. 7.

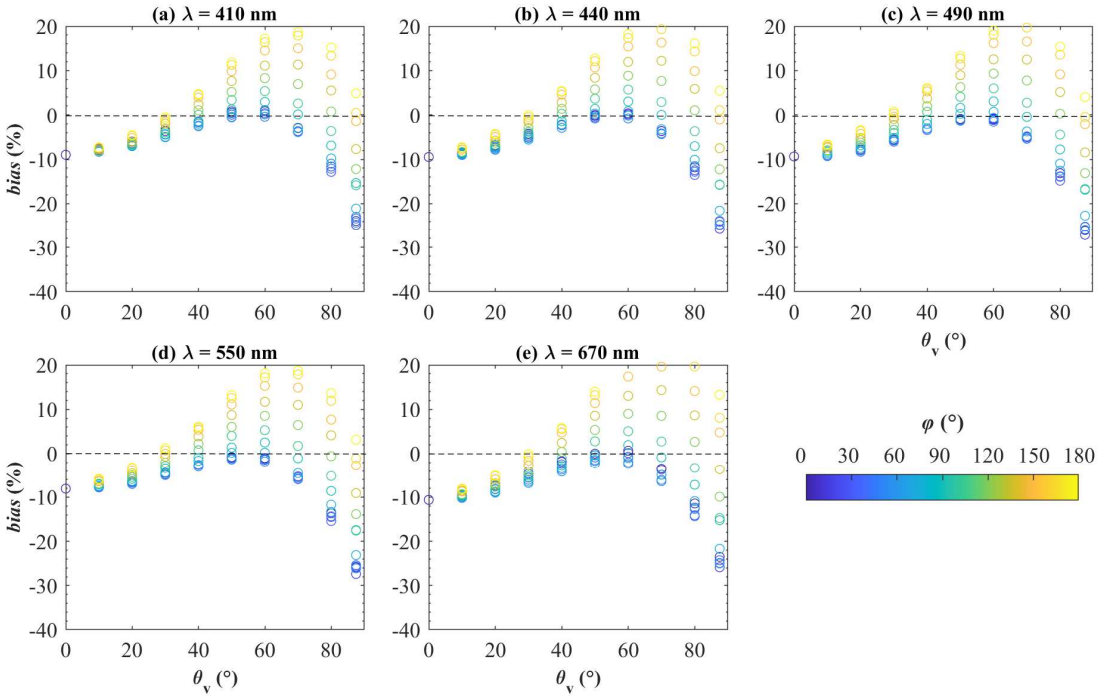

Fig. 7. The *bias* of derived $\alpha_w(\lambda)$ from ρ_w-α_w with input $R_{rs}(\lambda)$ of various viewing geometries (i.e., different combinations of viewing zenith angle θ_v and viewing azimuth angle relative to the solar plane φ). The marker color indicates the input φ.

As shown in Fig. 7, for small θ_v scenarios (< 40°), the *bias* of estimated $\alpha_w(\lambda)$ using different angular $R_{rs}(\lambda)$ as input is generally within ±10%. However, for large θ_v scenarios (> 60°), the *bias* of estimated $\alpha_w(\lambda)$ could range from −30% to 20%. As concluded from Fig. 6, ρ_w-α_w could also have larger uncertainties for high solar-zenith angle scenarios. Results in Fig. 6 and Fig. 7 suggest the strong bidirectionality of $R_{rs}(\lambda)$, and the performance of ρ_w-α_w is highly dependent on the angle of the input $R_{rs}(\lambda)$. Although presently satellite $R_{rs}(\lambda)$ product is corrected to nadir-viewed $R_{rs}(\lambda)$ (Gordon and Wang, 1994; Wang, 2006), the present in-water BRDF correction scheme used for producing nadir-viewed $R_{rs}(\lambda)$ product is based on Chl

(Gordon et al., 1988; Morel and Gentili, 1993), which could introduce extra uncertainties to the nadir-viewed $R_{rs}(\lambda)$ (see Section 3.2.1). Also, using nadir-viewed $R_{rs}(\lambda)$ as input may result in slightly larger errors for ρ_w-α_w as shown in Fig. 7. Therefore, ρ_w-α_w could be used as a good approximation, while IOPs-α_w can provide improved estimations with uncertainties usually within ~3% (see Fig. 3).

3.3. Global distribution of spectral $\alpha_w(\lambda)$

To map the spatial distribution of spectral $\alpha_w(\lambda)$, global products of $R_{rs}(\lambda)$ and θ_s are required. Here, VIIRS monthly products of 2019, at a spatial resolution of 9 km, are selected as the desired input $R_{rs}(\lambda)$. The VIIRS monthly $R_{rs}(\lambda)$ product is composited from the Level-2 products, which are atmospherically corrected by NOAA Multi-Sensor Level-1 to Level-2 (MSL12) ocean color data processing system using the combined near-infrared and shortwave-infrared (NIR-SWIR) algorithm (Jiang and Wang, 2014; Wang and Shi, 2007; Wang, 2007). Note that all Level-2 $R_{rs}(\lambda)$ products are corrected to $R_{rs}(\lambda)$ viewed at nadir with the Sun at the zenith before being composited to the monthly data. For the solar-zenith angle required to calculate $\alpha_w(\lambda)$, we calculate the monthly average θ_s at local noontime for the global ocean that matches the geographic coordinates in the VIIRS product. By implementing IOPs-α_w to VIIRS data, spectral $\alpha_w(\lambda)$ maps at local noontime are obtained and presented in Fig. 8. Here, the VIIRS monthly product of March 2019 is used for a demonstration.

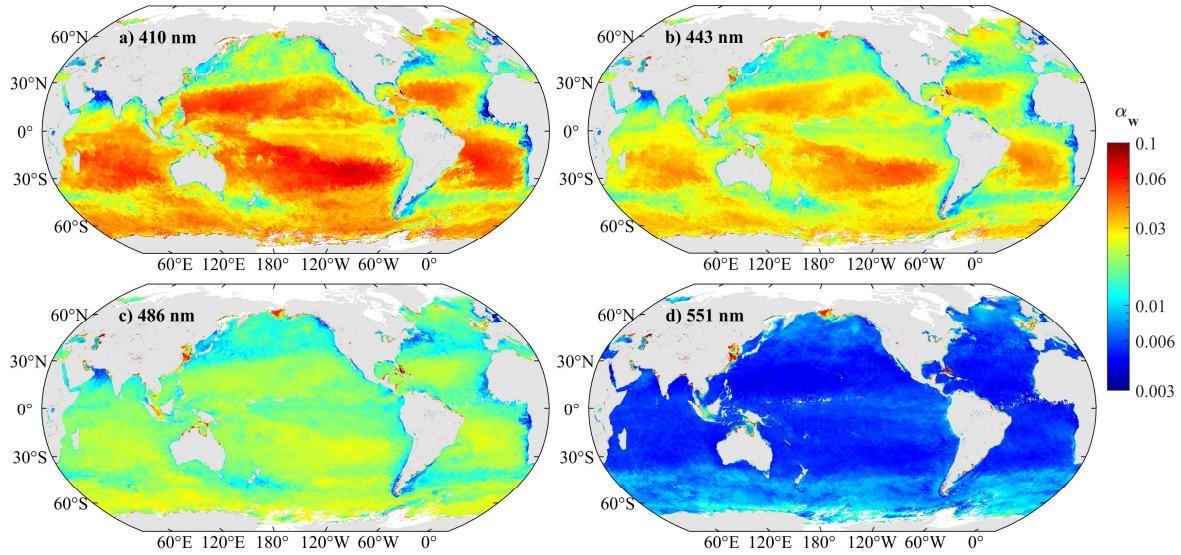

Fig. 8. Global distribution of spectral $\alpha_w(\lambda)$ derived from IOPs-α_w using VIIRS monthly composite data of March 2019.

As shown in Fig. 8, $\alpha_w(\lambda)$ are characteristic of strong spatial variation and wavelength dependence, with spatial distribution pattern generally consistent with that of $R_{rs}(\lambda)$ (see Fig. 6 of Wang et al. (2009)). Specifically, $\alpha_w(\lambda)$ are much higher at short wavelengths in open oceans and decrease toward longer wavelengths. The mapping product of $\alpha_w(671)$ is not shown because $\alpha_w(671)$ values are very small in open oceans. For turbid coastal and inland waters, opposite trends of $\alpha_w(\lambda)$ are observed, where $\alpha_w(\lambda)$ values are small at blue bands and increase toward longer wavelengths.

3.4. Broadband α_{w_VIS} and its monthly variations

Broadband albedo is often of greater interest than spectral albedo in climate models. Thus, the coefficients of conversion from narrowband $\alpha_w(\lambda)$ to α_{w_VIS} (i.e., k_i in Eq. (13)) need to be specified. In this study, the conversion coefficients are optimized for VIIRS bands using *SynData* and tabulated in Table 1. Conversion coefficients for other operational satellite

sensors are also provided in Table 1 to address different band configurations, including the Moderate Resolution Imaging Spectroradiometer (MODIS) onboard the Aqua, the Ocean and Land Colour Instrument (OLCI) onboard the Sentinel-3A, and the Operational Land Imager (OLI) onboard the Landsat 8. The robustness of these conversion coefficients is evaluated by comparing the converted α_{w_VIS} to the known α_{w_VIS} calculated by Eq. (12) using the simulated dataset, where MAPD of converted α_{w_VIS} is generally around 1% for all sensors. The slope and R^2 values for the linear regression between converted and 'true' α_{w_VIS} are also computed with both values close to 1 for all sensors (not shown in Table 1).

Table 1. Optimized empirical coefficients (Coeff.) for spectral $\alpha_w(\lambda)$ to α_{w_VIS} conversion for various satellite sensors.

	VIIRS		**MODIS**		**OLCI**		**OLI**	
	Band (nm)	Coeff.	Band (nm)	Coeff.	Band (nm)	Coeff.	Band (nm)	Coeff.
k_1	410	0.0793	412	0.0581	413	0.1111		
k_2	443	0.1105	443	0.1730	443	0.0839	443	0.2004
k_3	486	0.1765	488	0.1188	490	0.1884	482	0.1899
k_4	551	0.2962	547	0.3187	560	0.2827	562	0.2770
k_5	671	0.4155	678	0.4197	674	0.3966	655	0.3090
k_0		2E-05		4E-05		2E-05		-3E-05
MAPD (%)		1.0		1.2		1.0		0.9

Fig. 9 shows the monthly distribution of α_{w_VIS} derived from IOPs-α_w using VIIRS monthly composite data in 2019. To more explicitly show the monthly variation of α_{w_VIS}, we also select three regions of interest from the global ocean, highlighted in Fig. 9l, and calculate the median α_{w_VIS} of each region, along with the standard deviation. Specifically, two subregions in the South Pacific Gyre (SPG, 124°W–104°W; 32°S–22°S) and the Yangtze

Estuary (YE, 120.7°E–123°E; 29.5°N–32.5°N) selected as waters in gyres and turbid coastal waters appear to have larger α_{w_VIS} than those in other open ocean waters. A subregion in the Tropical Pacific Ocean (TPO, 175°W–145°W; 2°S–2°N) is also selected for its relatively small seasonal variability of α_{w_VIS}. The monthly variations of the median α_{w_VIS} in SPG, YE, and TPO are presented in Fig. 10.

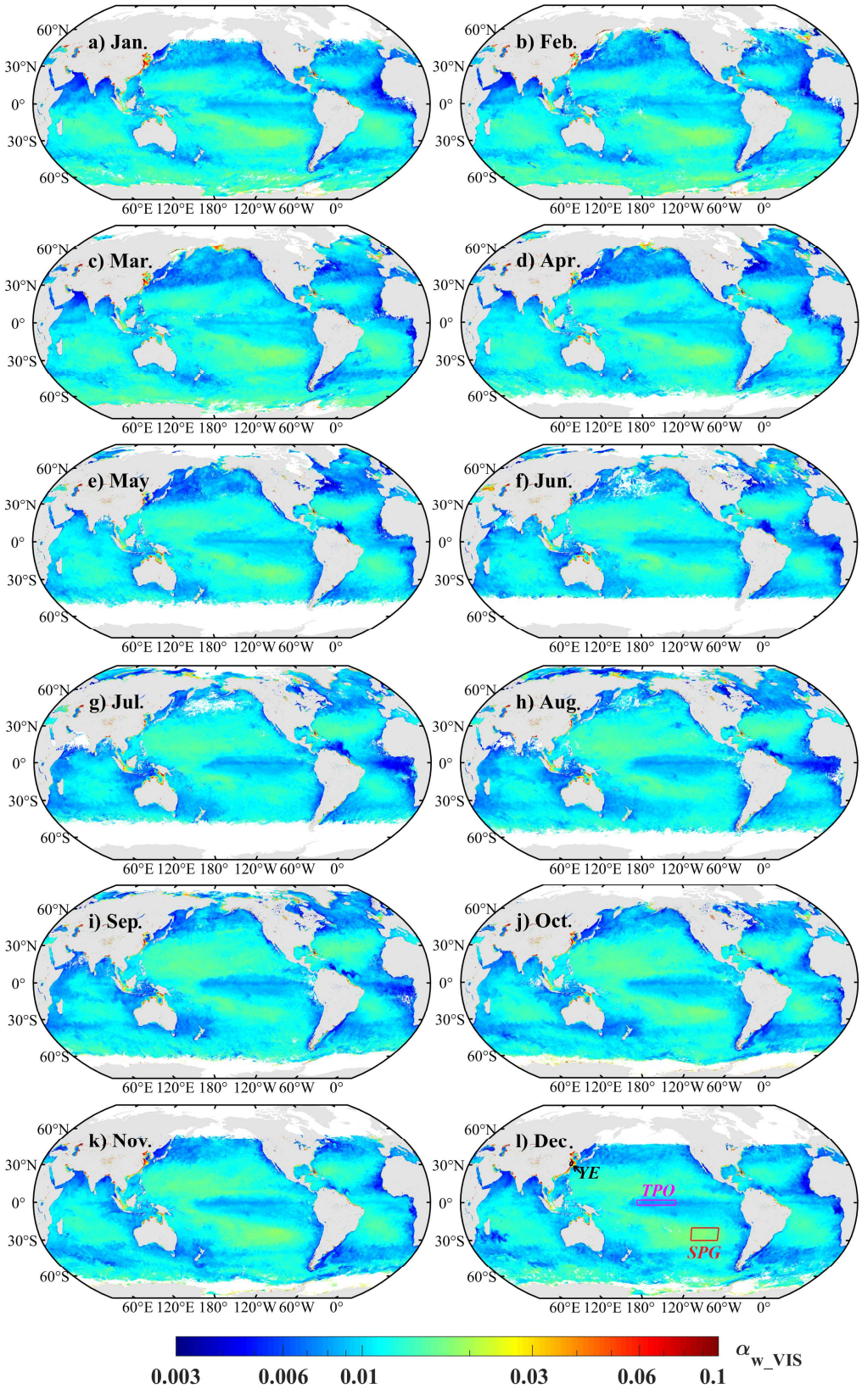

Fig. 9. Monthly variation of global α_{w_VIS} in 2019 mapped by IOPs-α_w using VIIRS composite data. The red, magenta and black boxes in panel (l) highlight the locations of three regions of interest in the South Pacific Gyre (SPG), the Tropical Pacific Ocean (TPO), and the Yangtze Estuary (YE), respectively.

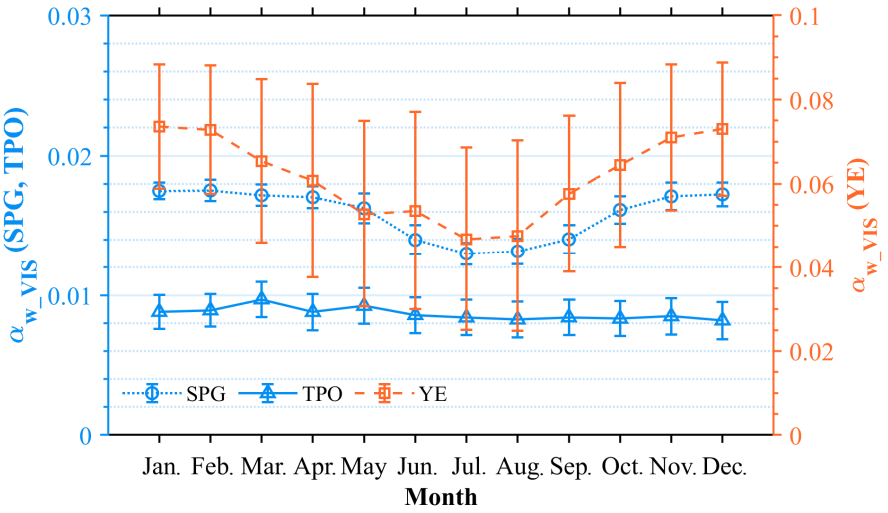

Fig. 10. Monthly variation of the median α_{w_VIS} in SPG, TPO, and YE in 2019, with the error bars showing the standard deviation. The locations of the three subregions are highlighted in Fig. 9l.

It is clearly demonstrated in Fig. 9 that α_{w_VIS} is characteristic of strong spatial-temporal variability. For the open ocean, α_{w_VIS} could vary by an order of magnitude from 0.003 to 0.02, with larger α_{w_VIS} observed mainly in the ocean gyres and the Southern Ocean. Seasonal variation of α_{w_VIS} is also predominant in subtropical gyre waters and coastal oceans. As shown in Fig. 10, α_{w_VIS} in SPG peaked in austral summer (~0.018) and reached the minimum in austral winter (~0.012) in 2019, with the amplitude of α_{w_VIS} variation around 0.006. For turbid coastal waters, such as the Yangtze Estuary, α_{w_VIS} is much larger (up to ~0.09) and shows strong seasonal variations, with an amplitude of ~0.07. α_{w_VIS} in TPO does not show an apparent seasonal pattern, with α_{w_VIS} generally varying between 0.009 and 0.01 across all months in 2019. Note that the distance to the equator might affect the mean water-incident radiance distribution, which could potentially contribute to the seasonal cycle of α_{w_VIS} observed in Fig. 10. For instance, the mean distances between the three subregions and the equator are 3000 km, 3400 km, and 0 km for SPG, YE, and TPO, respectively, whereas α_{w_VIS} in TPO shows a very weak seasonal variation. Nevertheless, results in Fig. 9 and Fig. 10

532 highlight the necessity of considering the spatial-temporal variation of α_{w_VIS} in climate
533 models as it could vary by orders of magnitude in global oceans in different regions and
534 seasons.

535 4. Discussion

536 *4.1. Robustness of IOPs-α_w*

537 The validity of IOPs-α_w depends on whether the angular distribution of $R_{rs}(\lambda)$ for all
538 viewing directions can be accurately reconstructed from IOPs under various scenarios that
539 could be encountered in natural waters. Therefore, the robustness and applicability of the
540 default *G*-LUT need to be evaluated. It appears that the developed *G*-LUT is robust for all
541 solar-zenith angle scenarios, as derived $\alpha_w(\lambda)$ from all θ_s cases are quite consistent and are not
542 biased for high θ_s cases (see Fig. 2). Thus, the developed IOPs-α_w scheme and *G*-LUT should
543 be applicable to measurements under all θ_s scenarios. It is worthy to point out that in remote
544 sensing applications, present satellite $R_{rs}(\lambda)$ products are subject to large uncertainties at high
545 θ_s scenarios (He et al., 2018; Mikelsons et al., 2020), which will introduce uncertainties to the
546 derived $\alpha_w(\lambda)$. However, obtaining accurate satellite $R_{rs}(\lambda)$ is out of the scope of this study.
547 Thus, in the following text, we mainly evaluate the impacts of wind speed and particle
548 scattering phase function on the derived $\alpha_w(\lambda)$ using IOPs-α_w.

549 4.2.1. Impact of wind speed

550 Wind speed is a key parameter in the Chl-α_w as it affects the reflection–refraction term $\Re$
551 in Eq. (8) (Morel et al., 2002). However, it is also reported that, for not very large solar- and

552 sensor-zenith angles, $\Re$ is nearly independent of w (Gordon, 2005; Wang, 2006). Here, we
553 investigate preliminarily the effects of wind speed using HydroLight simulations. Specifically,
554 in addition to the default *G*-LUT that employs all simulations for LUT development, three
555 separate *G*-LUTs are also developed from *SynData* for screened simulations with wind speed
556 of 5, 10, and 15 m/s, respectively. The resultant *G*-LUTs are termed *G*-LUT-*w*5, *G*-LUT-*w*10,
557 and *G*-LUT-*w*15. Table 2 tabulates the MAPD values of derived $\alpha_w(\lambda)$ by IOPs-α_w with
558 different *G*-LUTs employed.

559 Table 2. MAPD and *bias* for $\alpha_w(\lambda)$ derived from IOP-α_w using different *G*-LUTs. The default *G*-LUT
560 employs all simulations, while the three other LUTs employ screened simulations with wind speed of 5,
561 10, and 15 m/s, respectively. The numbers within parentheses are the *bias*.

	MAPD (*bias*) (%)			
Wavelength (nm)	*G*-LUT (default)	*G*-LUT-*w*5	*G*-LUT-*w*10	*G*-LUT-*w*15
410	2.9 (2.0)	2.5 (0.8)	2.9 (1.9)	3.7 (3.4)
440	2.6 (1.8)	2.2 (0.5)	2.6 (1.7)	3.6 (3.3)
490	1.8 (1.1)	2.0 (0.1)	1.8 (1.0)	3.0 (2.6)
550	2.5 (2.0)	2.4 (1.1)	2.4 (2.0)	3.3 (3.2)
670	7.3 (7.1)	5.3 (4.8)	7.2 (7.0)	9.6 (9.5)

562

563 Results in Table 2 show that MAPD for $\alpha_w(\lambda)$ derived using different *G*-LUTs is in
564 general consistent, except for relatively larger MAPD for retrievals using *G*-LUT-*w*15.
565 However, using *G*-LUT-*w*15 only accounts for 1% ~ 2% increase of MAPD compared to that
566 using the default *G*-LUT, while using the other two *G*-LUTs generally changes MAPD by
567 less than 1%, except for $\alpha_w(671)$. Thus, we can conclude that IOPs-α_w is slightly dependent on
568 wind speed, and the impact of wind speed can usually be safely neglected, at least for the
569 simulated dataset of this study.

570 4.2.2. Impact of particle scattering phase functions

571 Particle volume scattering phase function (β, in sr^{-1}) determines the distribution of
572 photons scattering into different angles by particles suspended within the water column, and
573 hence affects the distribution of water-leaving radiance above the sea surface. Therefore, β
574 could affect the G values (Lee et al., 2011). Given that β varies largely in natural waters
575 (Sullivan and Twardowski, 2009; Twardowski et al., 2007; Zhang and Gray, 2015), it is not
576 practical to develop G-LUT for all possible scattering phase functions. Here we try to briefly
577 characterize the impact of β on the estimated $\alpha_w(\lambda)$ from IOPs-α_w. As a demonstration, we
578 applied IOPs-α_w to *SynData*-FF using the default G-LUT developed from *SynData* and
579 calculated MAPD for derived $\alpha_w(\lambda)$ for the five selected wavelengths (see Table 3).

580 Table 3. Statistics of derived $\alpha_w(\lambda)$ from IOPs-α_w for implementation in *SynData*-FF. Statistics of
581 derived $\alpha_w(\lambda)$ for *SynData* are also included for comparison.

	MAPD (*bias*) (%)	
Wavelength (nm)	$\alpha_w(\lambda)$	$\alpha_w(\lambda)$ (*SynData*)
410	4.1 (1.5)	2.9 (2.0)
440	3.7 (1.4)	2.6 (1.8)
490	2.8 (0.9)	1.8 (1.1)
550	2.4 (1.2)	2.5 (2.0)
670	6.3 (5.8)	7.3 (7.1)

582

583 Comparing to the estimated $\alpha_w(\lambda)$ in *SynData*, implementation of IOPs-α_w to *SynData*-FF
584 only result in slight increases in MAPD by ~1% for the derived $\alpha_w(\lambda)$ in most wavelengths
585 (see Table 3). Such increases in MAPD are relatively insignificant given the large difference
586 between the two particle scattering phase functions, where the particulate
587 backscattering-to-scattering ratio for β used in *SynData* is almost doubled compared to that in

588 *SynData*-FF (i.e., 1.83% vs. 1%). Therefore, it can be concluded that IOPs-α_w is only slightly
589 dependent on β, and the impact of β can usually be safely neglected.

590 4.2.3. Impact of Raman scattering and chlorophyll fluorescence

591 The existence of Raman scattering could result in elevated reflectance in the green-red
592 domain (Gordon, 2014), while the existence of chlorophyll fluorescence typically increases
593 the reflectance around 683 nm (Gower et al., 1999; Hoge and Swift, 1987). Therefore, Raman
594 scattering and chlorophyll fluorescence could result in larger $\alpha_w(\lambda)$ in the longer wavelengths,
595 and it is necessary to investigate the impacts of these two inelastic scattering on the
596 performance of IOPs-α_w. Thus, we applied IOPs-α_w to the *SynData*-RF dataset and calculated
597 the statistical metrics of derived $\alpha_w(\lambda)$, with results shown in Fig. 11. Note that only three
598 wavelengths (440, 550, and 680 nm) are selected here as demonstrations. The first two
599 wavelengths represent the blue-green domain, while 680 nm is representative of the red
600 domain and is also close to the chlorophyll fluorescence peak. For proper comparisons,
601 simulations in the *SynData* were screened for the same IOPs and wind speed as that used in
602 *SynData*-RF, and a subset of *SynData* matching *SynData*-RF was obtained, termed
603 *SynData*-sub hereafter. Statistical metrics of derived $\alpha_w(\lambda)$ for the *SynData* subset are also
604 included in Fig. 11 for comparisons.

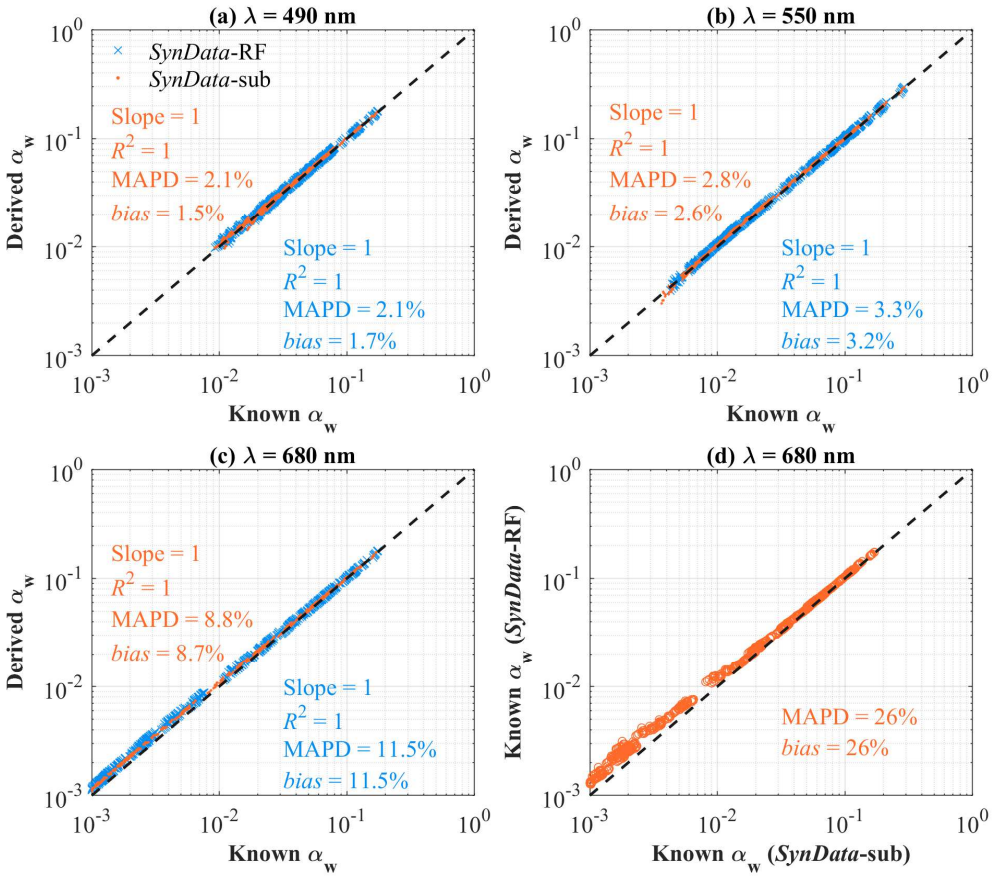

Fig. 11. Evaluation of the derived $\alpha_w(\lambda)$ from IOPs-α_w for *SynData*-RF and *SynData*-sub, with panels (a)–(c) showing the results of derived $\alpha_w(\lambda)$ at 490, 550, and 680 nm, respectively. Panel (d) shows the comparison of known $\alpha_w(680)$ in the *SynData*-RF and *SynData*-sub datasets.

As shown in Fig. 11, for the blue-green bands, the MAPD and *bias* of derived $\alpha_w(\lambda)$ from IOPs-α_w are very comparable for *SynData*-RF and *SynData*-sub with the respective differences in MAPD and *bias* are less than 0.5%, which is expected as $R_{rs}(\lambda)$ in the blue-green domain is only slightly affected by Raman scattering. For $\alpha_w(\lambda)$ at 680 nm, where Raman scattering and chlorophyll fluorescence together contribute to ~26% increase of the $\alpha_w(\lambda)$ in terms of *bias* (see Fig. 11d), the implementation of IOPs-α_w to *SynData*-RF results in only slightly larger uncertainties in the estimated $\alpha_w(\lambda)$, with MAPD of derived $\alpha_w(680)$ increasing from 8.8% in *SynData*-sub to 11.5% in *SynData*-RF. The increment of 2.7% in

MAPD and 2.8% in *bias* for the derived $\alpha_w(680)$ suggest that the current IOPs-α_w, developed from *SynData*, is applicable for waters with the existence of Raman scattering and chlorophyll fluorescence. More importantly, as shown in Fig. 11c, the larger values of MAPD and *bias* for derived $\alpha_w(680)$ are mainly due to an overestimation of $\alpha_w(680)$ for simulations representing oceanic waters (i.e., small $\alpha_w(680)$ values). Thus, the relatively larger uncertainties in $\alpha_w(680)$ could have limited impacts on the computed broadband water-leaving albedo, such as α_{w_VIS}, given the relatively small values of $\alpha_w(680)$ in oceanic waters.

It is recognized that the existence of Raman scattering and chlorophyll fluorescence would result in larger uncertainties in the derived IOPs from $R_{rs}(\lambda)$ (Lee et al., 2005; Lee et al., 2015). However, despite the large uncertainties in the derived IOPs, IOPs-α_w, or specifically QAA_Lee11, can ensure an optical closure between the input $R_{rs}(\lambda)$ and modeled $R_{rs}(\lambda)$ of the same viewing angle, where contributions of Raman scattering and chlorophyll fluorescence are included. In other words, the modeled $R_{rs}(680)$ at nadir is the same as that from Hydrolight simulations. As discussed in Section 3.1, uncertainties in the modeled $R_{rs}(680)$ at other viewing angles are mainly attributed to the modeled BRDF variation of $R_{rs}(\lambda)$, which is only slightly dependent on the accuracy of derived IOPs. Therefore, the estimated $\alpha_w(680)$ by IOPs-α_w for *SynData*-RF is just slightly different from that for *SynData*-sub (see Fig. 11c). It is worthy to point out that IOPs can also be derived from Eq. (6) using spectral optimization (Werdell et al., 2013; Yu et al., 2016), but these approaches are not recommended for the estimation of $\alpha_w(\lambda)$ since an optical closure of $R_{rs}(\lambda)$ cannot be guaranteed.

For satellite remote sensing, because here the focus is the estimation of $\alpha_w(\lambda)$, which is

directly related to $R_{rs}(\lambda)$ (see Eq. (5)), not the IOPs, it is not recommended to correct the effects of Raman scattering and chlorophyll fluorescence for the retrieval of IOPs with QAA_Lee11. Note that CDOM fluorescence also results in elevated water-leaving reflectance, especially in the ultraviolet-blue domain (Lee et al., 1994; Vodacek et al., 1994), but its impact on the estimated $\alpha_w(\lambda)$ can also be neglected when IOPs-α_w is employed, the same way as the impacts of Raman scattering and chlorophyll fluorescence.

4.2. Underrepresented contribution of α_{w_VIS} by previous schemes

As IOPs in *SynData* were determined randomly from Chl, evaluation with *SynData* may not provide a fair assessment of Chl-α_w. Here, we implement Chl-α_w to the VIIRS monthly data and compare the resultant spatial distribution of derived α_{w_VIS} with that from IOPs-α_w, which could imply the difference of both schemes in natural waters. As an example, both IOPs-α_w and Chl-α_w are applied to the VIIRS monthly data of March 2019, with generated α_{w_VIS} mapping products presented in Fig. 12. Input wind speed for Chl-α_w is set to 10 m/s, while input θ_s for both schemes is the average θ_s at noontime in March 2019. For easier interpretation of their difference, the ratio of derived α_{w_VIS} by Chl-α_w and that by IOPs-α_w is also computed and included in Fig. 12d. The mapping product of derived α_{w_VIS} by Jin11 is not presented as it is comparable with Chl-α_w. The mapping product of α_{w_VIS} derived from the ρ_w-α_w scheme is also included in Fig. 12c for comparison, with Fig. 12e showing the ratio of α_{w_VIS} derived from ρ_w-α_w to α_{w_VIS} derived from IOPs-α_w.

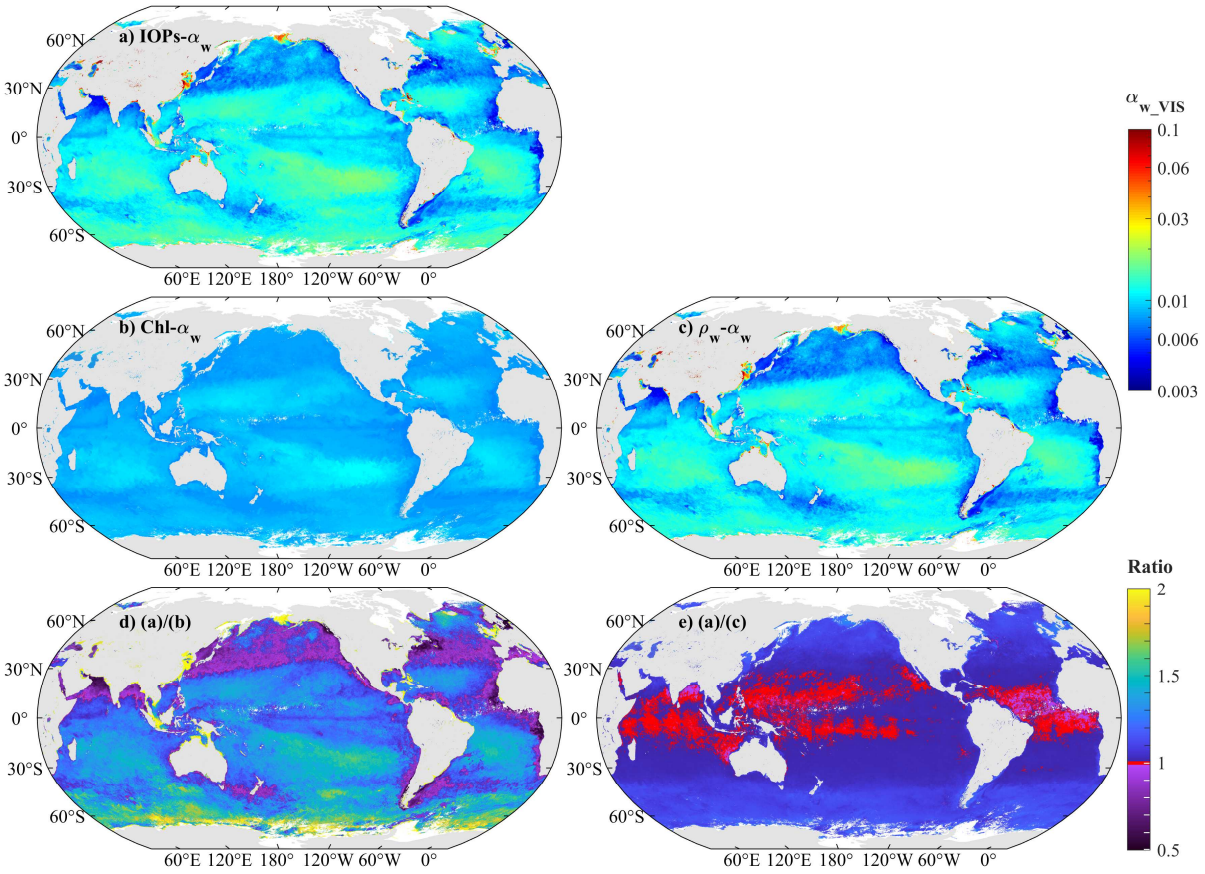

Fig. 12. Global mapping products of α_{w_VIS} in March 2019 derived from (a) IOPs-α_w, (b) Chl-α_w, and (c) ρ_w-α_w using the VIIRS data. Panels (d) and (e) show the ratio of (a) to (b), and (a) to (c), respectively. The red color in panels (d) and (e) indicates pixels where estimated α_{w_VIS} from different schemes agree with each other (ratio between 0.99 and 1.01).

Comparing to IOPs-α_w, Chl-α_w overall yields smaller α_{w_VIS} in most of the global ocean, except for waters in some coastal regions and the northern hemisphere above the latitudinal line of 30°N (see dark pixels in Fig. 12d). For the ocean gyres and the Southern Ocean, collectively accounting for more than 40% of the global ocean in the surface area, α_{w_VIS} derived from IOPs-α_w is almost twice as high as that from Chl-α_w. As discussed in section 3.2.1, a fixed Chl-IOPs relationship could introduce large errors in the estimated α_{w_VIS} for global applications. For turbid coastal waters where Chl-α_w is deemed inapplicable, IOPs-α_w

671 still provides reasonable spatial distribution of α_{w_VIS}, with α_{w_VIS} over 0.1 in extremely turbid
672 waters (such as the Yangtze Estuary), which is consistent with the estimations by Fogarty et al.
673 (2018). In contrast, the estimated α_{w_VIS} by Chl-α_w is less than 0.01 in these waters, which is
674 difficult to justify. It is worthy to point out that in extremely turbid waters, such as the
675 Yangtze Estuary where the suspended sediment concentration could be over 2000 mg/L (Yu et
676 al., 2019a), strong backscattering by particles in the NIR domain (elevated reflectance) could
677 contribute substantially to the water-leaving albedo, resulting in a much higher proportion of
678 water-leaving albedo to α_{broad}. It is thus required to include the NIR contribution by IOPs-α_w
679 for future applications in these waters.

680 The spatial variation of the α_{w_VIS} ratio (Fig. 12d) confirms that it is inappropriate to use
681 fixed Chl-IOPs relationships to infer IOPs for global oceans. Note that $\alpha_w(\lambda)$ is governed by
682 total absorption and backscattering coefficients, not individual seawater constituents. In
683 addition to the large variations of the Chl-specific absorption and backscattering coefficients
684 of suspended particles, the relative proportion of CDOM to Chl also varies largely in the
685 global ocean (Morel et al., 2010), which introduces additional uncertainties to the inferred $a(\lambda)$
686 by Chl. Note that the fraction of CDOM to Chl is considered a constant in Morel and
687 Maritorena (2001), which could vary significantly in natural waters (Morel et al., 2010; Morel
688 and Gentili, 2009). As expressed in Eq. (8), $\alpha_w(\lambda)$ derived from Chl-α_w is dependent on the
689 ratio of total backscattering to total absorption coefficients. Thus, underestimation of CDOM
690 contribution results in larger α_w, and vice versa. For instance, pixels with dark colors in Fig.
691 12d are coincident with high CDOM-to-Chl proportion waters, as shown in Fig. 1b of Morel

et al. (2010). Given that IOPs can be semi-analytically derived from ocean color measurements, it is unnecessary to infer IOPs from Chl as extra uncertainties will be introduced.

The resultant α_{w_VIS} map derived from the ρ_w-α_w scheme is overall comparable with that from the IOPs-α_w scheme in both the spatial distribution and the magnitude of α_{w_VIS}, particularly for the low latitude regions. It shows that ρ_w-α_w scheme is a good approximation for deriving $\alpha_w(\lambda)$. As shown in Fig. 12e, the difference between estimated α_{w_VIS} from ρ_w-α_w and IOPs-α_w are usually within ~10% in low latitude oceans (e.g., 30°S – 30°N), and ρ_w-α_w overall predicts smaller α_{w_VIS} compared to that from IOPs-α_w. Consistent with Fig. 6, it can be found that the underestimation of α_{w_VIS} is particularly significant in high latitude oceans, corresponding to high noontime solar-zenith angle. For instance, estimated α_{w_VIS} from ρ_w-α_w may be underestimated by ~40% compared with those derived from IOPs-α_w for waters approaching polar regions. In addition, ρ_w-α_w tends to underestimate α_{w_VIS} in coastal waters, which further limits its global applications. Given that an isotropic distribution of $L_w(\lambda)$ is rarely encountered in natural waters (Morel and Gentili, 1993), which is also confirmed in Fig. 7, it is desirable to use the semi-analytical IOPs-α_w scheme for accurate $\alpha_w(\lambda)$ computations.

4.3. Contribution of α_{w_VIS} to α_{broad} and impact factors

The significance of α_{w_VIS} relies on its relative contribution to α_{broad}, which is the desired parameter in climate models. Many previous schemes of α_{broad} simply ignored the contribution of α_{w_VIS}. Even for the schemes taking account of water-leaving irradiance (Feng et al., 2016; Jin et al., 2011; Séférian et al., 2018), the assessments underrepresent or misrepresent the

713 contribution of α_{w_VIS} to α_{broad} due to their underestimation of $\alpha_w(\lambda)$. For instance, Feng et al.
714 (2016) concluded that α_{w_VIS} contributes less than 10% to α_{broad} in oceanic waters, while Jin et
715 al. (2011) suggested that α_{w_VIS} has limited spatial variations and a constant value of 0.006 can
716 be used to calculate α_{broad} for global oceans. However, results of this study show that
717 Chl-based α_w schemes could underestimate α_{w_VIS} by up to 50% in oceanic waters (see Fig.
718 12), thus undermining the contribution of α_{w_VIS} to α_{broad}. Based on the global distribution and
719 the magnitude of α_{w_VIS} derived from IOPs-α_w (e.g., Fig. 12a), it is fair to conclude that
720 neither the spatial variation of α_{w_VIS} nor the contribution of α_{w_VIS} to α_{broad} shall be negligible.

721 Due to the absence of field measurements, especially when measuring $\alpha_w(\lambda)$ is not yet
722 practical, HydroLight simulations are used here to preliminarily examine the relative
723 contribution of α_{w_VIS} to α_{broad} and the potential impact factors. Scatter plots of the ratio
724 between α_{w_VIS} and α_{VIS} (broadband α in the visible domain) in *SynData* are presented in Fig.
725 13, with three different symbols representing three different values of wind speed and the
726 color scale representing the variation in solar-zenith angle. Consistent with previous
727 suggestions, θ_s is the dominant factor determining the ratio of α_{w_VIS} to α_{VIS}, as surface
728 Fresnel reflectance increases rapidly with the increase of solar-zenith angle (Payne, 1972).
729 Wind speed, on the other hand, has very limited impacts on $\alpha_{w\_VIS}/\alpha_{VIS}$, except for high θ_s
730 cases. For the bluish symbols in Fig. 13, where θ_s is generally less than 45°, simulations with
731 the same IOPs but different w almost overlap. For high θ_s cases, higher w results in larger
732 $\alpha_{w\_VIS}/\alpha_{VIS}$, which can be explained as increasing w (roughened sea surface) could result in
733 small surface Fresnel reflectance under high θ_s scenarios (Jin et al., 2011).

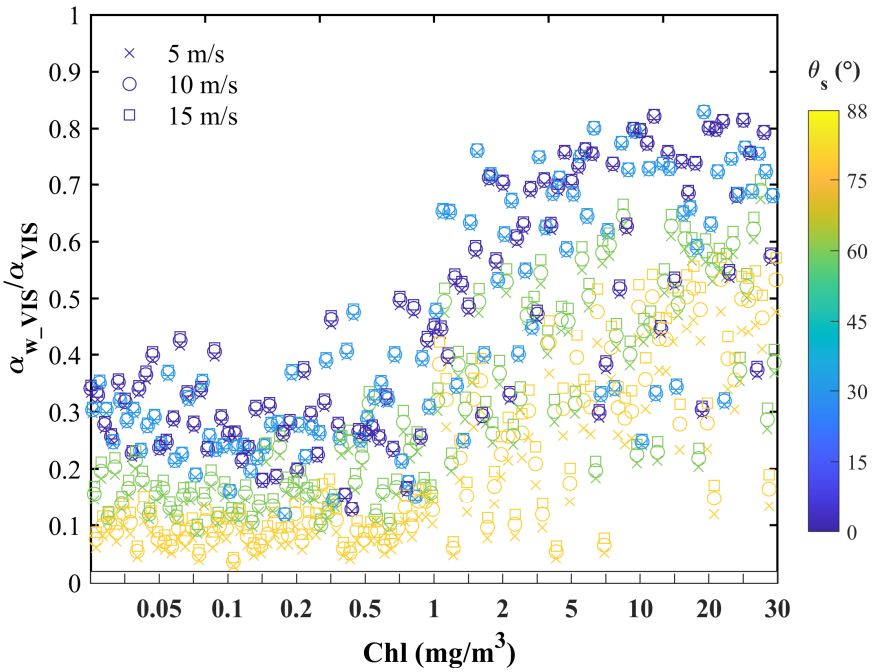

Fig. 13. The ratio of α_{w_VIS} to α_{VIS} in response to different inputs of solar-zenith angle, wind speeds, and Chl. For conciseness, every tenth simulation from the total number of 12,000 simulations in *SynData* are plotted here.

Quantitatively, α_{w_VIS} could contribute over 40% to α_{VIS} in oceanic waters (Chl < 0.2 mg/m^3) for small solar-zenith angles, and the contribution of α_{w_VIS} would be increased to over 80% in productive waters for the simulated dataset of this study (see Fig. 13). To understand the contribution of water-leaving albedo to α_{broad}, the ratio of the broadband α_w in the shortwave domain α_{w_broad} to α_{broad} is desired. By definition, α_{w_broad} can be calculated as

$$\alpha_{w\_broad} = \frac{\int_{200}^{3000} \alpha_w(\lambda) E_d(0^+,\lambda)}{\int_{200}^{3000} E_d(0^+,\lambda)}. \quad (16)$$

Given that visible radiation accounts for 42.3% of the total solar energy reaching Earth's surface (Gibson, 2003), i.e., $\int_{400}^{700} E_d(0^+,\lambda) = 0.423 \times \int_{200}^{3000} E_d(0^+,\lambda)$, one would expect that α_{w_broad} is larger than $\alpha_{w\_VIS}/0.423$, as $\int_{200}^{3000} \alpha_w(\lambda) E_d(0^+,\lambda)$ is greater than $\int_{400}^{700} \alpha_w(\lambda) E_d(0^+,\lambda)$ due to contributions of water-leaving reflectance from the ultraviolet (UV) and near-infrared (NIR) domains. In addition, it is suggested that the values of α_{broad} are comparable with α_{VIS} in

most natural waters with Chl < 3 mg/m^3 (see Table 1 of Ohlmann et al. (2000)). Thus, the ratio of $\alpha_{w\_broad}/\alpha_{broad}$ would be greater than 0.423 $\alpha_{w\_VIS}/\alpha_{VIS}$. According to Fig. 13, it is safe to conclude that α_{w_broad} could contribute up to 20% to α_{broad} in oceanic waters for small solar-zenith angles, which is much higher compared with the previous estimations by Feng et al. (2016) and Jin et al. (2011).

As $\alpha_w(\lambda)$ is generally a function of $R_{rs}(\lambda)$, $\alpha_w(\lambda)$ in the UV domain could be an important component of α_{w_broad} in oceanic waters, while $\alpha_w(\lambda)$ in the NIR domain are not negligible in extremely turbid waters. As a demonstration of $\alpha_w(\lambda)$ contribution in the UV domain, we re-calculated α_{w_VIS} for 350 – 700 nm following Eq. (12), the ratio of new α_{w_VIS} to α_{VIS} could increase by ~6.7% based on the *SynData*-sub for simulations with Chl < 0.2 mg/m^3. In other words, the ratio of α_{w_broad} to α_{broad} only increase by ~1.3% in oceanic waters when $\alpha_w(\lambda)$ in the UV domain is considered (i.e., from ~20% to ~21.3%). Thus, the use of α_{w_VIS} could provide sufficient understandings of the contribution of α_{w_broad} to α_{broad} regarding its spatial-temporal variations. However, further incorporation of $\alpha_w(\lambda)$ in both the UV and NIR domains is certainly preferred for more accurate quantification of α_{w_broad}, especially when VIIRS $R_{rs}(\lambda)$ products at both the UV and NIR domains can be acquired (Barnes et al., 2021; Wang et al., 2020).

Note that HydroLight simplifies the impact of wind speed on surface reflectance, such as reflectance of wind-induced foams and whitecaps are not considered (Mobley and Sundman, 2016), suggesting that the calculated α_{VIS} from HydroLight simulations would be smaller than that measured in natural waters for the same observational condition. However, the ~20%

770 contribution of α_{w_VIS} to α_{broad} in oceanic waters could be reasonable for low wind speed
771 scenarios where whitecap reflectance can be neglected (Koepke, 1984). Thus, results
772 presented in this study highlight that the contribution of α_{VIS} to α_{broad} cannot be neglected,
773 especially for small θ_s and w scenarios, when the solar radiation and upwelling irradiance
774 assume the highest values.

775 ## 5. Conclusions

776 Many efforts acknowledged the contribution of $\alpha_w(\lambda)$ to broadband ocean surface albedo
777 (Jin et al., 2002; Payne, 1972), but these studies obtained questionable $\alpha_w(\lambda)$ of the global
778 oceans due to the use of Chl-based schemes (Feng et al., 2016; Jin et al., 2011; Séférian et al.,
779 2018). The proposed IOPs-α_w scheme in this study has shown significantly improved
780 accuracy in the estimation of $\alpha_w(\lambda)$ compared with Chl-based schemes. More importantly,
781 IOPs-α_w has significantly broader applicability and can provide satisfying estimations of $\alpha_w(\lambda)$
782 for both oceanic and coastal waters. The resulted $\alpha_w(\lambda)$ from IOPs-α_w is found slightly
783 dependent on particle scattering phase function, wind speed, and solar-zenith angle, at least
784 for the simulated dataset (assuming accurate $R_{rs}(\lambda)$ can be derived). Further efforts are still
785 required for more rigorous evaluations, especially with field measurements.

786 Although results in this study are primarily based on numerical simulations, the
787 significance of IOPs-α_w is highlighted in its implementation to VIIRS data, where reasonable
788 global distribution and seasonal pattern of $\alpha_w(\lambda)$ are presented. Comparison with previous
789 studies shows that the Chl-based scheme could underestimate α_{w_VIS} by more than 50% in
790 oceanic waters, thus undermine the relative contribution of water-leaving albedo to ocean

surface albedo. Results of this study show that α_{w_VIS} could contribute up to 20% to α_{broad} in oceanic waters under small solar-zenith angles. The magnitude and the spatial-temporal variation of α_{w_VIS} derived from IOPs-α_w suggest that neither the spatial variability of α_{w_VIS} nor the contribution of α_{w_VIS} to α_{broad} shall be neglected.

MATLAB scripts for IOPs-α_w, the associated *G*-LUT, and the monthly α_{w_VIS} products derived using IOPs-α_w in 2019 from VIIRS composite data are all made available online (https://github.com/oceanopticsxmu/osaw) to facilitate further evaluation and assessment.

Disclosures

The authors declare no conflicts of interest.

Acknowledgments

This work was supported by the National Natural Science Foundation of China (#42006162, #41941008, #41890803, #41776184, and #41830102), the National Key Research and Development Program of China (#2016YFC1400906), China Postdoctoral Science Foundation Grant (#2019M662234), the Outstanding Postdoctoral Scholarship of the State Key Laboratory of Marine Environmental Science at Xiamen University, the Fundamental Research Funds for the Central Universities (#20720200028), the Joint Polar Satellite System funding for the NOAA ocean color calibration and validation (Cal/Val) project, and the University of Massachusetts Boston. We thank Dr. Xianqiang He and Dr. Zhehai Shang for their insightful comments and suggestions. The scientific results and conclusions, as well as any views or opinions expressed herein, are those of the author(s) and do not necessarily

reflect those of NOAA or the Department of Commerce.

References:

Abraham, J.P., Baringer, M., Bindoff, N., Boyer, T., Cheng, L., Church, J., Conroy, J., Domingues, C., Fasullo, J., & Gilson, J. (2013). A review of global ocean temperature observations: Implications for ocean heat content estimates and climate change. *Reviews of Geophysics, 51*, 450-483.

Barnes, B.B., Hu, C., Bailey, S.W., Pahlevan, N., & Franz, B.A. (2021). Cross-calibration of MODIS and VIIRS long near infrared bands for ocean color science and applications. *Remote Sensing of Environment, 260*, 112439.

Behrenfeld, M.J., & Falkowski, P.G. (1997). Photosynthetic rates derived from satellite‐based chlorophyll concentration. *Limnology and Oceanography, 42*, 1-20.

Bender, F.A.-M., Rodhe, H., Charlson, R.J., Ekman, A.M., & Loeb, N. (2006). 22 views of the global albedo—comparison between 20 GCMs and two satellites. *Tellus A: Dynamic Meteorology and Oceanography, 58*, 320-330.

Bricaud, A., Babin, M., Morel, A., & Claustre, H. (1995). Variability in the chlorophyll-specific absorption coefficients of natural phytoplankton: Analysis and parameterization. *Journal of Geophysical Research, 100*, 13321-13332.

Bricaud, A., Morel, A., & Prieur, L. (1981). Absorption by dissolved organic matter of the sea (yellow substance) in the UV and visible domains. *Limnology and Oceanography, 26*, 43-53.

Briegleb, B.P., Minnis, P., Ramanathan, V., & Harrison, E. (1986). Comparison of regional clear-sky albedos inferred from satellite observations and model computations. *Journal of Climate and Applied Meteorology, 25*, 214-226.

Carder, K.L., Chen, F.R., Lee, Z.P., Hawes, S.K., & Kamykowski, D. (1999). Semianalytic Moderate-Resolution Imaging Spectrometer algorithms for chlorophyll a and absorption with bio-optical domains based on nitrate-depletion temperatures. *Journal of Geophysical Research-Oceans, 104*, 5403.

Chang, G.C., & Dickey, T.D. (2004). Coastal ocean optical influences on solar transmission and radiant heating rate. *Journal of Geophysical Research: Oceans, 109*, C01020.

Cox, C., & Munk, W. (1954). Measurement of the roughness of the sea surface from photographs of the sun's glitter. *Journal of the Optical Society of America, 44*, 838-850.

Faizal, M., & Rafiuddin Ahmed, M. (2011). On the ocean heat budget and ocean thermal energy conversion. *International Journal of Energy Research, 35*, 1119-1144.

842 Feng, Y., Liu, Q., Qu, Y., & Liang, S. (2016). Estimation of the ocean water albedo from remote
843 sensing and meteorological reanalysis data. *IEEE Transactions on Geoscience and Remote*
844 *Sensing, 54*, 850-868.

845 Fogarty, M., Fewings, M., Paget, A., & Dierssen, H. (2018). The influence of a sandy substrate,
846 seagrass, or highly turbid water on albedo and surface heat flux. *Journal of Geophysical Research:*
847 *Oceans, 123*, 53-73.

848 Fournier, G.R., & Forand, J.L. (1994). Analytic phase function for ocean water. *In Proc. SPIE 2258*,
849 *Ocean Optics XII*, pp: 194-201, doi.org/10.1117/12.190063.

850 Gibson, J. (2003). UVB radiation: definition and characteristics. *USDA/CSU, Available*
851 *online:https://uvb.nrel.colostate.edu/UVB/publications/uvb_primer.pdf.*

852 Gordon, H.R. (2005). Normalized water-leaving radiance: revisiting the influence of surface
853 roughness. *Applied Optics, 44*, 241-248.

854 Gordon, H.R. (2014). Influence of Raman scattering on the light field in natural waters: a simple
855 assessment. *Optics Express, 22*, 3675-3683.

856 Gordon, H.R., Brown, O.B., Evans, R.H., Brown, J.W., Smith, R.C., Baker, K.S., & Clark, D.K.
857 (1988). A Semianalytic Radiance Model of Ocean Color. *Journal of Geophysical*
858 *Research-Atmospheres, 93*, 10909-10924.

859 Gordon, H.R., & Wang, M. (1994). Influence of oceanic whitecaps on atmospheric correction of
860 ocean-color sensors. *Applied Optics, 33*, 7754-7763.

861 Gower, J.F.R., Doerffer, R., & Borstad, G.A. (1999). Interpretation of the 685nm peak in water-leaving
862 radiance spectra in terms of fluorescence, absorption and scattering, and its observation by
863 MERIS. *International Journal of Remote Sensing, 20*, 1771-1786.

864 Gupta, S.K., Ritchey, N.A., Wilber, A.C., Whitlock, C.H., Gibson, G.G., & Stackhouse Jr, P.W. (1999).
865 A climatology of surface radiation budget derived from satellite data. *Journal of Climate, 12*,
866 2691-2710.

867 Hansen, J., Russell, G., Rind, D., Stone, P., Lacis, A., Lebedeff, S., Ruedy, R., & Travis, L. (1983).
868 Efficient three-dimensional global models for climate studies: Models I and II. *Monthly Weather*
869 *Review, 111*, 609-662.

870 He, X., Stamnes, K., Bai, Y., Li, W., & Wang, D. (2018). Effects of Earth curvature on atmospheric
871 correction for ocean color remote sensing. *Remote Sensing of Environment, 209*, 118-133.

872 Henderson-Sellers, A., & Wilson, M.F. (1983). Surface albedo data for climatic modeling. *Reviews of*
873 *Geophysics, 21*, 1743-1778.

874 Hense, I., Stemmler, I., & Sonntag, S. (2017). Ideas and perspectives: climate-relevant marine

biologically driven mechanisms in Earth system models. *Biogeosciences, 14*, 403-413.

Hoge, F.E., & Swift, R.N. (1987). Ocean color spectral variability studies using solar-induced chlorophyll fluorescence. *Applied Optics, 26*, 18-21.

Hu, C., Lee, Z., & Franz, B. (2012). Chlorophyll a algorithms for oligotrophic oceans: A novel approach based on three-band reflectance difference. *Journal of Geophysical Research: Oceans, 117*, C01011.

Huot, Y., Morel, A., Twardowski, M., Stramski, D., & Reynolds, R. (2008). Particle optical backscattering along a chlorophyll gradient in the upper layer of the eastern South Pacific Ocean. *Biogeosciences, 5*, 495-507.

IOCCG (2000). Remote Sensing of Ocean Colour in Coastal, and Other Optically-Complex, Waters. *Sathyendranath, S. (ed.), Reports of the International Ocean-Colour Coordinating Group, No.3*, IOCCG, Dartmouth, NS, Canada.

IOCCG (2006). Remote Sensing of Inherent Optical Properties: Fundamentals, Tests of Algorithms, and Applications. *Lee, Z. P. (ed.), Reports of the International Ocean-Colour Coordinating Group, No. 5*, IOCCG, Dartmouth, NS, Canada.

IOCCG Protocol Series (2018). Inherent Optical Property Measurements and Protocols: Absorption Coefficient. *Neeley, A. R. and Mannino, A. (eds.), IOCCG Ocean Optics and Biogeochemistry Protocols for Satellite Ocean Colour Sensor Validation, Volume 1.0*, IOCCG, Dartmouth, NS, Canada.

Jiang, L., & Wang, M. (2014). Improved near-infrared ocean reflectance correction algorithm for satellite ocean color data processing. *Optics Express, 22*, 21657-21678.

Jin, Z., Charlock, T.P., & Rutledge, K. (2002). Analysis of broadband solar radiation and albedo over the ocean surface at COVE. *Journal of Atmospheric and Oceanic Technology, 19*, 1585-1601.

Jin, Z., Charlock, T.P., Smith Jr, W.L., & Rutledge, K. (2004). A parameterization of ocean surface albedo. *Geophysical Research Letters, 31*, L22301.

Jin, Z., Qiao, Y., Wang, Y., Fang, Y., & Yi, W. (2011). A new parameterization of spectral and broadband ocean surface albedo. *Optics Express, 19*, 26429-26443.

Kasten, F., & Czeplak, G. (1980). Solar and terrestrial radiation dependent on the amount and type of cloud. *Solar energy, 24*, 177-189.

Koepke, P. (1984). Effective reflectance of oceanic whitecaps. *Applied Optics, 23*, 1816-1824.

Laws, E.A. (1997). Mathematical methods for oceanographers: An introduction. John Wiley & Sons.

Lee, Z., Carder, K.L., & Arnone, R.A. (2002). Deriving inherent optical properties from water color: a multiband quasi-analytical algorithm for optically deep waters. *Applied Optics, 41*, 5755-5772.

Lee, Z., Carder, K.L., Hawes, S.K., Steward, R.G., Peacock, T.G., & Davis, C.O. (1994). Model for the interpretation of hyperspectral remote-sensing reflectance. *Applied Optics, 33*, 5721-5732.

Lee, Z., & Hu, C. (2006). Global distribution of Case-1 waters: An analysis from SeaWiFS measurements. *Remote Sensing of Environment, 101*, 270-276.

Lee, Z., Rhea, W.J., Arnone, R., & Goode, W. (2005). Absorption coefficients of marine waters: Expanding multiband information to hyperspectral data. *IEEE Transactions on Geoscience and Remote Sensing, 43*, 118-124.

Lee, Z., Wei, J., Voss, K., Lewis, M., Bricaud, A., & Huot, Y. (2015). Hyperspectral absorption coefficient of "pure" seawater in the range of 350–550 nm inverted from remote sensing reflectance. *Applied Optics, 54*, 546-558.

Lee, Z.P., Carder, K.L., Marra, J., Steward, R.G., & Perry, M.J. (1996). Estimating primary production at depth from remote sensing. *Applied Optics, 35*, 463-474.

Lee, Z.P., Du, K., Voss, K.J., Zibordi, G., Lubac, B., Arnone, R., & Weidemann, A. (2011). An inherent-optical-property-centered approach to correct the angular effects in water-leaving radiance. *Applied Optics, 50*, 3155-3167.

Li, J., Scinocca, J., Lazare, M., McFarlane, N., Von Salzen, K., & Solheim, L. (2006). Ocean surface albedo and its impact on radiation balance in climate models. *Journal of Climate, 19*, 6314-6333.

Liang, S. (2001). Narrowband to broadband conversions of land surface albedo I: Algorithms. *Remote Sensing of Environment, 76*, 213-238.

Loisel, H., & Morel, A. (1998). Light scattering and chlorophyll concentration in case 1 waters: A reexamination. *Limnology and Oceanography, 43*, 847-858.

Loisel, H., & Stramski, D. (2000). Estimation of the inherent optical properties of natural waters from the irradiance attenuation coefficient and reflectance in the presence of Raman scattering. *Applied Optics, 39*, 3001-3011.

Maritorena, S., Siegel, D.A., & Peterson, A.R. (2002). Optimization of a semianalytical ocean color model for global-scale applications. *Applied Optics, 41*, 2705--2714.

Mikelsons, K., Wang, M., & Jiang, L. (2020). Statistical evaluation of satellite ocean color data retrievals. *Remote Sensing of Environment, 237*, 111601.

Mobley, C.D. (1994). Light and water: radiative transfer in natural waters. Academic press.

Mobley, C.D., Gentili, B., Gordon, H.R., Jin, Z., Kattawar, G.W., Morel, A., Reinersman, P., Stamnes,

K., & Stavn, R.H. (1993). Comparison of numerical models for computing underwater light fields. *Applied Optics, 32*, 7484-7504.

Mobley, C.D., Stramski, D., Paul Bissett, W., & Boss, E. (2004). Optical modeling of ocean waters: Is the case 1-case 2 classification still useful? *Oceanography, 17*, 60-67.

Mobley, C.D., & Sundman, L.K. (2016). Hydrolight 5.3 Ecolight 5.3 Users' Guide. *Sequoia Scientific Inc.*

Morel, A., Antoine, D., & Gentili, B. (2002). Bidirectional reflectance of oceanic waters: accounting for Raman emission and varying particle scattering phase function. *Applied Optics, 41*, 6289-6306.

Morel, A., Claustre, H., & Gentili, B. (2010). The most oligotrophic subtropical zones of the global ocean: similarities and differences in terms of chlorophyll and yellow substance. *Biogeosciences, 7*, 3139-3151.

Morel, A., & Gentili, B. (1991). Diffuse reflectance of oceanic waters: its dependence on Sun angle as influenced by the molecular scattering contribution. *Applied Optics, 30*, 4427-4438.

Morel, A., & Gentili, B. (1993). Diffuse reflectance of oceanic waters. II. Bidirectional aspects. *Applied Optics, 32*, 6864-6879.

Morel, A., & Gentili, B. (1996). Diffuse reflectance of oceanic waters. III. Implication of bidirectionality for the remote-sensing problem. *Applied Optics, 35*, 4850-4862.

Morel, A., & Gentili, B. (2009). A simple band ratio technique to quantify the colored dissolved and detrital organic material from ocean color remotely sensed data. *Remote Sensing of Environment, 113*, 998-1011.

Morel, A., Gentili, B., Claustre, H., Babin, M., Bricaud, A., Ras, J., & Tieche, F. (2007). Optical properties of the "clearest" natural waters. *Limnology and Oceanography, 52*, 217-229.

Morel, A., & Maritorena, S. (2001). Bio-optical properties of oceanic waters: A reappraisal. *Journal of Geophysical Research: Oceans, 106*, 7163-7180.

Morel, A., & Prieur, L. (1977). Analysis of variations in ocean color. *Limnology and Oceanography, 22*, 709-722.

O'Reilly, J.E., Maritorena, S., Mitchell, B.G., Siegel, D.A., Carder, K.L., Garver, S.A., Kahru, M., & McClain, C. (1998). Ocean color chlorophyll algorithms for SeaWiFS. *Journal of Geophysical Research-Oceans, 103*, 24937-24953.

Ohlmann, J.C., Siegel, D.A., & Mobley, C.D. (2000). Ocean radiant heating. Part I: Optical influences. *Journal of Physical Oceanography, 30*, 1833-1848.

970 Payne, R.E. (1972). Albedo of the sea surface. *Journal of the Atmospheric Sciences, 29*, 959-970.

971 Petzold, T.J. (1972). Volume scattering functions for selected ocean waters. Scripps Institution of
972 Oceanography La Jolla Ca Visibility Lab.

973 Pope, R.M., & Fry, E.S. (1997). Absorption spectrum (380 –700 nm)of pure water. II. Integrating
974 cavity measurements. *Applied Optics, 36*, 8710-8723.

975 Reynolds, R.A., Stramski, D., & Mitchell, B.G. (2001). A chlorophyll‐dependent semianalytical
976 reflectance model derived from field measurements of absorption and backscattering coefficients
977 within the Southern Ocean. *Journal of Geophysical Research: Oceans, 106*, 7125-7138.

978 Roesler, C.S., & Perry, M.J. (1995). In situ phytoplankton absorption, fluorescence emission, and
979 particulate backscattering spectra determined from reflectance. *Journal of Geophysical Research:*
980 *Oceans, 100*, 13279-13294.

981 Séférian, R., Baek, S., Boucher, O., Dufresne, J.-L., Decharme, B., Saint-Martin, D., & Roehrig, R.
982 (2018). An interactive ocean surface albedo scheme (OSAv1. 0): formulation and evaluation in
983 ARPEGE-Climat (V6. 1) and LMDZ (V5A). *Geoscientific Model Development, 11*, 321-338.

984 Shi, W., & Wang, M. (2019). A blended inherent optical property algorithm for global satellite ocean
985 color observations. *Limnology and Oceanography: Methods, 17*, 377-394.

986 Stramska, M., Stramski, D., Hapter, R., Kaczmarek, S., & Stoń, J. (2003). Bio-optical relationships
987 and ocean color algorithms for the north polar region of the Atlantic. *Journal of Geophysical*
988 *Research: Oceans, 108*, 3143, doi:10.1029/2001JC001195.

989 Sullivan, J.M., & Twardowski, M.S. (2009). Angular shape of the oceanic particulate volume
990 scattering function in the backward direction. *Applied Optics, 48*, 6811-6819.

991 Taylor, J., Edwards, J., Glew, M., Hignett, P., & Slingo, A. (1996). Studies with a flexible new
992 radiation code. II: Comparisons with aircraft short‐wave observations. *Quarterly Journal of the*
993 *Royal Meteorological Society, 122*, 839-861.

994 Twardowski, M., Claustre, H., Freeman, S., Stramski, D., & Huot, Y. (2007). Optical backscattering
995 properties of the" clearest" natural waters. *Biogeosciences, 4*, 1041-1058.

996 Vodacek, A., Green, S.A., & Blough, N.V. (1994). An experimental model of the solar‐stimulated
997 fluorescence of chromophoric dissolved organic matter. *Limnology and Oceanography, 39*, 1-11.

998 Wang, M. (2006). Effects of ocean surface reflectance variation with solar elevation on normalized
999 water-leaving radiance. *Applied Optics, 45*, 4122-4128.

1000 Wang, M., & Shi, W. (2007). The NIR-SWIR combined atmospheric correction approach for MODIS
1001 ocean color data processing. *Optics Express, 15*, 15722-15733.

1002 Wang, M., & Son, S. (2016). VIIRS-derived chlorophyll-a using the ocean color index method.
1003 *Remote Sensing of Environment, 182*, 141-149.

1004 Wang, M.H. (2007). Remote sensing of the ocean contributions from ultraviolet to near-infrared using
1005 the shortwave infrared bands: simulations. *Applied Optics, 46*, 1535-1547.

1006 Wang, M.H., Son, S., & Shi, W. (2009). Evaluation of MODIS SWIR and NIR-SWIR atmospheric
1007 correction algorithms using SeaBASS data. *Remote Sensing of Environment, 113*, 635-644.

1008 Wang, Y., Lee, Z., Wei, J., Shang, S., Wang, M., & Lai, W. (2020). Extending satellite ocean color
1009 remote sensing to the near-blue ultraviolet bands. *Remote Sensing of Environment, 253*, 112228,
1010 doi.org/10.1016/j.rse.2020.112228.

1011 Wei, G., Lee, Z., Wu, X., Yu, X., Shang, S., & Letelier, R. (2021). Impact of Temperature on
1012 Absorption Coefficient of Pure Seawater in the Blue Wavelengths Inferred from Satellite and In
1013 Situ Measurements. *Journal of Remote Sensing, 2021*, 1-13, doi.org/10.34133/2021/9842702.

1014 Werdell, P.J., Franz, B.A., Bailey, S.W., Feldman, G.C., Boss, E., Brando, V.E., Dowell, M., Hirata, T.,
1015 Lavender, S.J., & Lee, Z. (2013). Generalized ocean color inversion model for retrieving marine
1016 inherent optical properties. *Applied Optics, 52*, 2019-2037.

1017 Yu, X., Lee, Z., Shang, Z., Lin, H., & Lin, G. (2021). A simple and robust shade correction scheme for
1018 remote sensing reflectance obtained by the skylight-blocked approach. *Optics Express, 29*,
1019 470-486.

1020 Yu, X., Lee, Z., Shen, F., Wang, M., Wei, J., Jiang, L., & Shang, Z. (2019a). An empirical algorithm to
1021 seamlessly retrieve the concentration of suspended particulate matter from water color across
1022 ocean to turbid river mouths. *Remote Sensing of Environment, 235*, 111491,
1023 doi.org/10.34133/2021/9842702.

1024 Yu, X., Lee, Z., Wei, J., & Shang, S. (2019b). Impacts of pure seawater absorption coefficient on
1025 remotely sensed inherent optical properties in oligotrophic waters. *Optics Express, 27*,
1026 34974-34984.

1027 Yu, X., Salama, M.S., Shen, F., & Verhoef, W. (2016). Retrieval of the diffuse attenuation coefficient
1028 from GOCI images using the 2SeaColor model: A case study in the Yangtze Estuary. *Remote*
1029 *Sensing of Environment, 175*, 109-119.

1030 Zhang, X., & Gray, D.J. (2015). Backscattering by very small particles in coastal waters. *Journal of*
1031 *Geophysical Research: Oceans, 120*, 6914-6926.

1032 Zhang, X., Hu, L., & He, M. (2009). Scattering by pure seawater: effect of salinity. *Optics Express, 17*,
1033 5698-5710.

1034